

Geochemistry, Geophysics, Geosystems®



RESEARCH ARTICLE

10.1029/2021GC010283

Key Points:

- Detailed structural and morphological analysis of the headwall area of the giant Sahara Slide Complex
- The headwall area was shaped by a series of individual slope failures over the last 60 kyr
- Failure occurs along multiple stratigraphic layers throughout the slope sediments

Correspondence to:

Q. Tang,
qinqin.tang@ifg.uni-kiel.de

Citation:

Tang, Q., Geersen, J., Düring, A., Unverricht, D., Schneider von Deimling, J., Lenz, K.-F., et al. (2022). Sequence of multiple slope failures in the headwall area of the giant Sahara Slide Complex at the NW African continental margin. *Geochemistry, Geophysics, Geosystems*, 23, e2021GC010283. <https://doi.org/10.1029/2021GC010283>

Received 1 DEC 2021

Accepted 3 MAR 2022

Sequence of Multiple Slope Failures in the Headwall Area of the Giant Sahara Slide Complex at the NW African Continental Margin

Q. Tang¹ , J. Geersen¹ , A. Düring¹, D. Unverricht¹ , J. Schneider von Deimling¹, K.-F. Lenz¹ , W. Li² , and S. Krastel¹

¹Institute of Geosciences, Kiel University, Kiel, Germany, ²South China Sea Institute of Oceanology, Chinese Academy of Sciences, Guangzhou, China

Abstract Submarine mega-slides involving hundreds of cubic kilometers of slope material pose a major threat due to their potential to destroy offshore infrastructure and trigger devastating tsunamis. The Sahara Slide Complex affected about 50,000 km² of the northwestern (NW) African continental margin. Previous studies focused either on its distal depositional zone or the uppermost headwall area, but failed in reconstructing the succession of individual slide events within the entire headwall area. New hydroacoustic data reveal a complex slide morphology including three main acoustic facies, large scale slide blocks, linear troughs, multiple glide planes and three major headwall scarps (the upper, southern and lower headwall). The evacuated slide scar hosts chaotic slide deposits that cover stratified sediments in the upper and southern headwall area, but are vertically stacked onto older slide deposits in the lower headwall area. Based on these observations, and dating of recently collected sediment samples, we reconstructed the history of slope failures that led to the formation of the structurally and morphologically complex headwall area of the Sahara Slide. Slope instability initiated when the lower headwall failed at ~60 kyr, followed by the failure of the northeastern upper headwall at ~14 kyr. Around 6 kyr, a major slide within the upper headwall area took place, followed by a series of smaller events within the southern and most-proximal upper headwall area. The youngest of these slides occurred around 2 kyr. This scenario suggests a long-lasting history of successive slope failures for the Sahara Slide Complex along the NW African continental slope.

Plain Language Summary Giant submarine landslides are a natural hazard, which can threaten marine infrastructure including seafloor communication cables, and potentially generate dangerous tsunami. The Sahara Slide Complex is a submarine landslide that affected an area of about 50,000 km² offshore the coast of northwestern Africa. It is important to know the mechanisms and the geological framework of the Sahara Slide Complex to better understand the risk of such large landslides to coastal populations and infrastructure. Therefore, we collected data for imaging the seafloor, understanding the structure below the seafloor and reconstructing ages of individual slide bodies. Three areas with submarine landslides were found in the headwall area of the Sahara Slide Complex. We observed landslide material and lined troughs on the seafloor. Our data show a long history of unstable slopes in the Sahara slide Complex area: it began around 60,000 years BP at the lower headwall, followed by the northeastern part of the upper headwall area at 14,000 years BP. The main slide of the upper headwall area occurred at 6,000 years BP. Slides in the southern headwall area and shallowest part of the upper headwall area appeared with the youngest slide at 2,000 years BP.

1. Introduction

Submarine landslides are commonly found along passive and active continental margins, seamounts, volcanic islands and other subaqueous slopes (Hühnerbach & Masson, 2004; Krastel et al., 2014; McAdoo et al., 2000). At passive continental margins, submarine landslides can be up to two orders of magnitude larger than those that occur on land (Masson et al., 2006). The evacuated slide scar forms a headwall area, while the mobilized sediments and rocks are usually referred to as mass-transport deposits (MTDs). Both, the headwall area and the MTDs are typical structural features for large submarine landslides (Krastel et al., 2018; Tappin et al., 2001). Some MTDs evacuated from the slide scar can develop into debris flows or turbidity currents, which can travel for thousands of kilometers down continental slopes into abyssal plains (Talling et al., 2007). These debris flows or turbidity currents may directly damage submarine infrastructure such as communication cables, offshore drilling

© 2022 The Authors.

This is an open access article under the terms of the [Creative Commons Attribution-NonCommercial License](#), which permits use, distribution and reproduction in any medium, provided the original work is properly cited and is not used for commercial purposes.

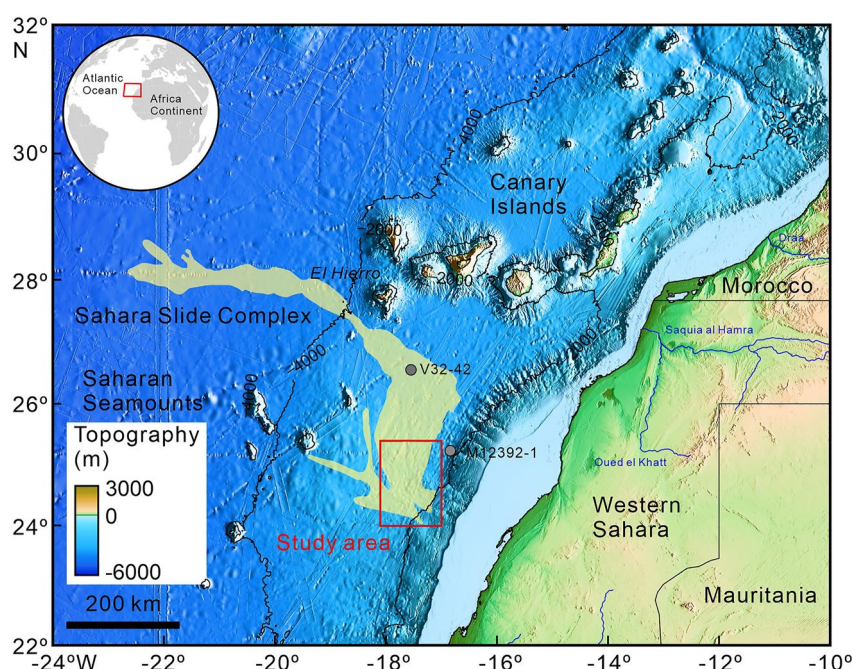


Figure 1. Map of the northwestern African continental margin based on the GEBCO2020 grid (GEBCO Compilation Group, 2020). The Sahara Slide Complex is marked in light yellow (modified after Krastel et al., 2018; Wynn et al., 2000). The red box marks the headwall area of the Sahara Slide Complex (study area). Gray circles mark locations of previously collected sediment-cores referred to in this manuscript (V32-42 and M12392-1).

platforms, and submerged pipelines (Carter et al., 2012; Piper et al., 2002; Schulten et al., 2019). The sudden mobilization of sediments and rocks during a submarine or coastal landslide can also trigger tsunamis that represent a significant threat to coastal areas. The 1998 Papua New Guinea tsunami, which was triggered by a submarine landslide (5–10 km³ in volume), reached a wave height of up to 15 m, and caused >2,200 fatalities (Tappin et al., 2001). The 2018 tsunami in Palu Bay was likely triggered by series of submarine landslides, and caused >2,000 fatalities (Pakoksung et al., 2019). These two recent landslide tsunamis were caused by relatively small submarine landslides compared to some of the mega-slides (hundreds of km³ in volume) which have occurred on passive continental margins. The well-known Storegga Slide occurred around 8 kyr off Norway, and involved around 3,000 km³ of slope sediment (Haflidason et al., 2004). It triggered an ocean basin wide tsunami (5–7 m of reconstructed run-up), the tsunami deposits of which were found in western Norway, northeastern Scotland and the Shetland Islands (Bondevik et al., 2005). The similar sized Trandjupet Slide on the continental slope off Norway, in contrast, did not trigger a significant tsunami (Laberg & Vorren, 2000). This emphasizes the need to understand the failure behavior of submarine landslides in order to assess landslide tsunami potential for different regions.

The northwestern (NW) African continental margin is home to a wide range of mass-wasting processes, including several prominent large-scale but infrequent submarine landslides (Krastel et al., 2018; Weaver et al., 2000). The Sahara Slide Complex (Figure 1) is one of these mega-slides, affecting about 50,000 km² of the seafloor (Georgiopolou et al., 2010; Krastel et al., 2018; Wynn et al., 2000), while the Storegga Slide influenced an area of 95,000 km² (Canals et al., 2004) with the run-out distance of up to 810 km (Micallef et al., 2007). Georgiopolou et al. (2010) suggested that the Sahara Slide Complex initiated as a slab-type failure creating two prominent headwalls. It then transformed into a debris flow, incorporating volcanoclastic materials when it passed south of the Canary Islands. This led to the formation of a two-phase debris flow: a basal volcanoclastic debris flow phase overlain by a pelagic debris flow phase. The low friction related to excess pore pressure in the volcanoclastic debris flow (sandy layer) may well explain the long run-out of 900 km of the Sahara Slide Complex (Gee et al., 1999; Georgiopolou et al., 2010). Embley (1982) suggested an age of 15–16 kyr for the Sahara Slide Complex based on sediment samples (core V32-42) within the slide pathway (Figure 1). Gee et al. (1999) revised

the age of the debris flow emplacement to ~60 kyr by dating of the dominant coccolith assemblages in the distal depositional part of the Sahara Slide Complex.

Most of the early studies on the Sahara Slide Complex focused on the distal depositional area (Gee et al., 1999; Georgiopoulou et al., 2009, 2010). The headwall area, in contrast, was only partially mapped with marine geophysical data and rarely sampled. Based on seismic reflection data from the headwall area, Georgiopoulou et al. (2007) suggested that differential compaction within an old landslide scarp may have triggered subsequent failures of the Sahara Slide. Recently collected sediment cores indicate a late Holocene reactivation within the headwall area of the Sahara Slide Complex (Georgiopoulou et al., 2009; Krastel et al., 2012), including a young failure at ~2 kyr in the upper headwall area (Li et al., 2017). From sub-bottom profiles and side-scan sonar data, there is indication that the upper headwall area was formed by retrogressive failure events associated with translational sliding and gravitational spreading (Li et al., 2017). The lack of similar data from the lower headwall area, however, made it challenging so far to develop a comprehensive understanding of the sequence of failures across the entire Sahara Slide Complex and the relation of the different headwall areas.

Major parts of the lower headwall and an additional, previously undescribed, headwall in the south (southern headwall area) were, for the first time, comprehensively mapped in 2019 during RV Maria S. Merian cruises MSM82/2 and MSM87. Combining all of the vintage and newly collected multibeam bathymetric data, sub-bottom profiles, and sediment cores, the specific objectives of our study are: (a) Describe the structure and morphology of the headwall area of Sahara Slide Complex; (b) Reconstruct the history of slope failures in the headwall area; (c) Assess potential preconditioning factors and implications for geohazards.

The results contribute to a better understanding of a submarine mega-slide which is a characteristic structural element at the NW African continental margin. Although representing a rare and infrequent event, the consequences of such a mega slide would be extreme.

2. Geological Setting

The passive NW African continental margin was formed during North Atlantic rifting in the Late Jurassic (Summerhayes et al., 1976; von Rad et al., 1982). It has an almost flat continental shelf with an average width of 40–60 km, increasing to a maximum width of >100 km off the Western Saharan coast (Figure 1). The shelf break is located around a water depth of 100–200 m. The continental slope is 50–250 km wide with slope gradients of 1–6° in water depth of 200–4,000 m while the continental rise is <1° steep beyond a water depth of 4,000 m (Wynn et al., 2000). Wynn et al. (2000) classified the NW African margin as a fine-grained clastic slope apron, with pelagic/hemipelagic background sediments overprinted by downslope gravity flows, and modified by along-slope bottom currents. The background hemipelagic sediments typically consist of carbonate-rich marls, silt, clay and oozes.

Aeolian dust input from the Sahara Desert dominates the terrestrial sediment input to the NW African continental margin. Terrestrial sediment input is linked with climate variability in the hinterland, with maximum input during deglaciations and high input during glacial times (Holz et al., 2004). The headwall area of the Sahara Slide Complex is located about 140 km off the Western Sahara Coast (Figure 1). River-sourced sediment supply to the region is minimal and almost no fluvial input occurred throughout the late Quaternary (Summerhayes et al., 1976). Average sedimentation rates for Holocene sediments on the upper slope are 5 cm/kyr (M12392-1 in Figure 1) (Müller & Suess, 1979). Oceanic upwelling driven by the northeastern trade winds results in a high primary productivity (21–35°N) (Cropper et al., 2014), which can cause high sedimentation rates exceeding 14.7 cm/kyr in places (Müller & Suess, 1979; Ruddiman et al., 1988).

Earthquakes are rare along the passive NW African continental margin, although moderate magnitude events ($4 \leq M \leq 6$) are sometimes recorded. They likely relate to old weak zones created during the opening of the Atlantic Ocean (Hayes & Rabinowitz, 1975). No recent major earthquakes ($M > 6$) affected the region of the Sahara Slide Complex, while there were some small events at the adjacent volcanic Canary Archipelago (Earthquake Catalog since 1959 from USGS: <https://earthquake.usgs.gov/earthquakes/search/>).

Table 1
Different Dataset Used in This Study

Cruise	Time	Data	Cruise report
Meteor 58/1	16 April 2003–12 May 2003	Sub-bottom profiles Sediment cores	H. Schulz et al. (2003)
Maria S. Merian 11/2	14 March 2009–09 March 2009	Multibeam bathymetric data Sub-bottom profiles	Bickert et al. (2011)
Poseidon 395	04 February 2010–19 February 2010	Sediment cores	Krastel et al. (2010)
Maria S. Merian 82/2	26 April 2019–14 May 2019	Multibeam bathymetric data Sub-bottom profiles Sediment cores	Krastel, Kinne, et al. (2019)
Maria S. Merian 87	16 November 2019–25 November 2019	Multibeam bathymetric data Sub-bottom profiles	Krastel, Barrett, et al. (2019)

3. Data and Methods

To reconstruct the history and evolution of the Sahara Slide Complex we used a combination of multibeam bathymetric data, sub-bottom profiles, and sediment cores (Table 1 and Figure 2). The bulk of multibeam bathymetric data were acquired during RV Maria S. Merian cruises MSM11/2 (Bickert et al., 2011), MSM82/2 (Krastel, Kinne, et al., 2019) and MSM87 (Krastel, Barrett, et al., 2019) with hull-mounted Kongsberg Simrad systems EM120 (MSM11/2) and EM122 (MSM82/2 and MSM87) (Figures 2a and 2b). The nominal sonar frequency is 12 kHz. The angular coverage is up to 150°, and each angular beam accuracy was 2° by 2°. Kongsberg Seapath system provides the combined motion, position and time data, which are transmitted to the Processing Unit of the multibeam echosounder to achieve real-time motion compensation in pitch, roll and yaw. All raw data were processed with MB-System software (Caress & Chayes, 2017: <https://www.mbari.org/products/research-software/mb-system/>). Sound velocities were measured with a Conductivity, Temperature, Depth probe during MSM 82/2 and an expendable sound velocimeter during MSM87. For MSM11/2, sound velocities were adjusted using the mbvelocity tool implemented in the MB-System software. The multibeam bathymetric data were gridded by using the splines with tension algorithm to a final grid with 150 m cell spacing in lateral direction.

Sub-bottom profiles were acquired during several cruises with RV Meteor (M58/1) (H. Schulz et al., 2003) and RV Maria S. Merian (MSM11/2, MSM82/2, MSM87). The high-resolution parametric ATLAS Parasound System DS3 (Atlas Hydrographic®) is a hull-mounted parametric echo sounder; the secondary low frequency (SLF) was set to 4 kHz through our cruises. The opening angle of the system is 4.5°. The system allows imaging of the uppermost 50–100 m of sediment at a sub-meter vertical resolution. The echogram sections were filtered with a wide band pass filter to improve the signal-to-noise ratio. We recorded the SLF data as compressed PS3 data format within a 200 m long reception window. Afterward the PS3 SLF data were converted to SGY-files using the ps32sgy tool (written by Hanno Keil, University of Bremen). The converted SGY data were analyzed and interpreted in IHS Kingdom®.

Gravity cores were acquired with a 5 m-long standard gravity corer during RV Maria S. Merian Cruise MSM82/2 (cores MSM82/2-34, MSM82/2-35 and MSM82/2-36). The new data were combined with information from previously collected gravity cores GeoB8532, GeoB8533, P395-04-1 and P395-07-1 (Georgiopolou et al., 2009, 2010; Krastel et al., 2010; Li et al., 2017) (Table 1 and Figure 2c). The new cores were studied by visual analysis, X-radiography and radiocarbon dating (^{14}C). Accelerated Mass Spectrometry ^{14}C -age dating of the planktonic foraminifera Globigerinoides ruber (Bonfardedi et al., 2018) was performed at the Leibniz Laboratory for Radiometric Dating and Stable Isotope Research at Kiel University. The Calib 704 and the Marine 13 calibration curve were applied to calibrate ^{14}C age to calendar years (Reimer et al., 2013); the reservoir age was set to ± 500 years (Mangerud & Gulliksen, 1975).

To calculate the volume of failed material, we summed the missing volume inside the slide scar (the evacuated volume) and the volume of the slide material that was deposited within the headwall area. The evacuated space (the volume of material moved downslope) is assumed as a wedge-shaped geometry (McAdoo et al., 2000) and

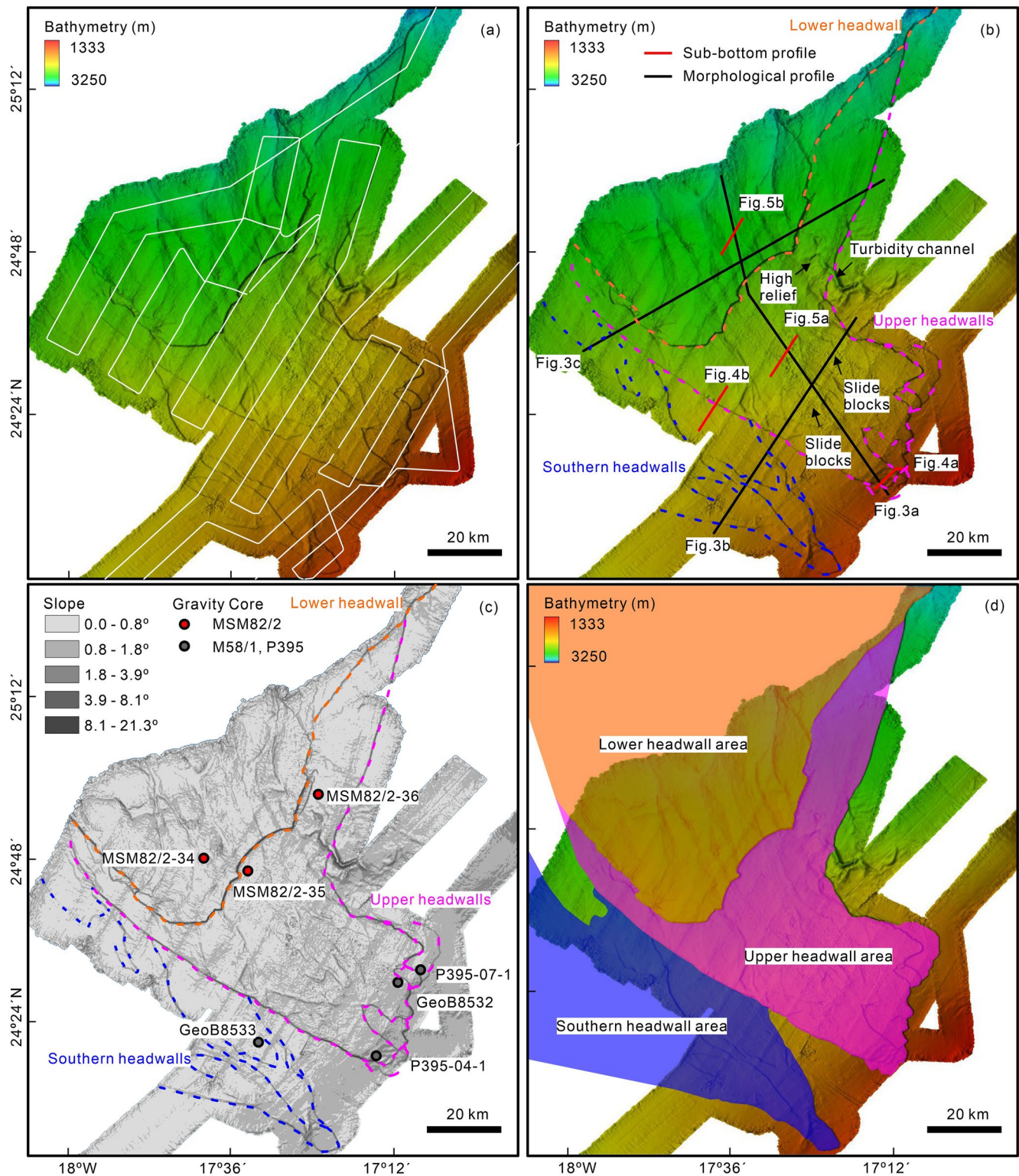


Figure 2. Morphological maps of the headwall area of the Sahara Slide Complex based on data collected during cruises MSM11/2, MSM82/2, and MSM87. (a) uninterpreted bathymetric data with white solid lines for the hydroacoustic survey lines. (b) interpreted bathymetric map with the three major headwalls marked by purple (upper headwall), blue (southern headwall) and orange (lower headwall) dashed lines. (c) slope gradient map with the three major headwalls. Circles mark the locations of cores taken during cruises M58/1 (gray), P395 (gray), and MSM82/2 (red). (d) spatial distribution of the upper, lower and southern headwall areas.

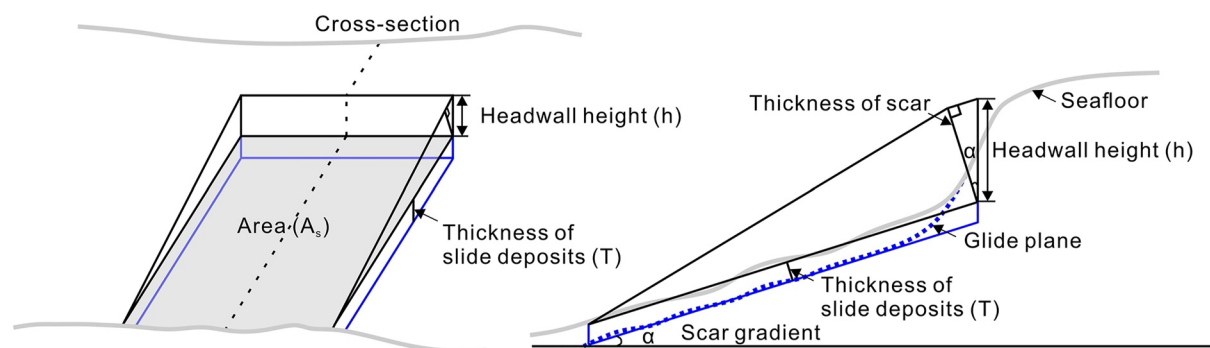


Figure 3. Schematic diagram for the volume estimation of failed material in the headwall area of the Sahara Slide Complex (modified from McAdoo et al., 2000). The volume of failed material includes the present evacuated space and slide deposits within the headwall area.

the slide deposits as a parallelogram solid (Figure 3). The gradient of the unfailed slope immediately adjacent to the failure is a close representation of the seafloor prior to slope failure (McAdoo et al., 2000). The volume of evacuated material was calculated by the area (A_s) and the thickness of the scar, in which the thickness of the scar is based on the mean headwall height (h) and the average scar gradient (α). The slide deposits' volume inside the slide scar was estimated by the area of the scar (A_s) and the mean thickness of the slide deposits (T). We derived the area of the scar, the headwall height, and the slope gradient within the scar from bathymetric data, and the thickness of the slide deposits from sub-bottom profiles. The failed material's volume (V_f) is then calculated as: $V_f = \frac{1}{2}(A_s)(h\cos\alpha) + A_sT$ (Figure 3).

4. Results

4.1. Morphology and Structure of the Headwalls

The different headwalls form a distinct staircase morphology with multiple scarps that can be traced over 30–210 km along the continental slope (Figures 2b and 4). In the sub-bottom data, the scarps show up as steps, and they usually intersect continuously layered acoustic reflections farther upslope from chaotic to transparent slide deposits farther downslope (Figure 5). We separate the scarps into the upper headwall, the southern headwall, and the lower headwall (Figures 2b and 2c). For simplicity, we do not distinguish between headwalls and sidewalls of the slide in the uppermost 150 km of the 900 km long Sahara Slide Complex, although some of the headwalls may represent lateral boundaries of the slide.

The upper headwall is located in water depths of 1,650–3,050 m (Figure 2b). In the most proximal region, it separates into multiple minor headwalls with a characteristic staircase morphology. The northern part of the upper headwall bends from northwest to northeast, and disappears at 3,030 m water depth when it intersects the lower headwall (Figure 2b). The height of the upper headwall ranges between 20 and 100 m with a slope gradient from 4° to 21° (Figures 2b, 2c, and 4). The size of the enclosed upper headwall area is ~3,200 km² with a mean slope gradient around 0.8° (Table 2 and Figure 2d).

The shallowest water depth of the adjacent southern headwall is around 1,640 m, which is similar to the upper headwall. The height of the southern headwall ranges between 5 and 30 m (Figures 2b, 4b, and 4c). Compared to the upper headwall, the southern headwall displays lower slope gradients between 2° and 8° (Figure 2c). The southern headwall also separates into multiple minor headwalls (5–15 m high) that are formed by steep escarpment (Figures 2b and 2c). Some of these minor headwalls form pronounced steps cutting reflectors in sub-bottom profiles, but lack a corresponding seafloor expression. The latter results from the fact that the seafloor scarps are degraded and overprinted by more proximal derived slide deposits (Figure 5b). The mean slope gradient of 0.7° within the southern headwall area is similar to the upper headwall area. Due to the lack of bathymetric data within the more proximal sections of the southern headwall area we can only give a minimum size for the enclosed region, which is around ~2,600 km² (Figure 2d).

The lower headwall is located between water depths of 2,580–3,120 m but likely continues into deeper waters where shipborne bathymetric data is lacking (Figure 2b). The lower headwall presents a distinct single and

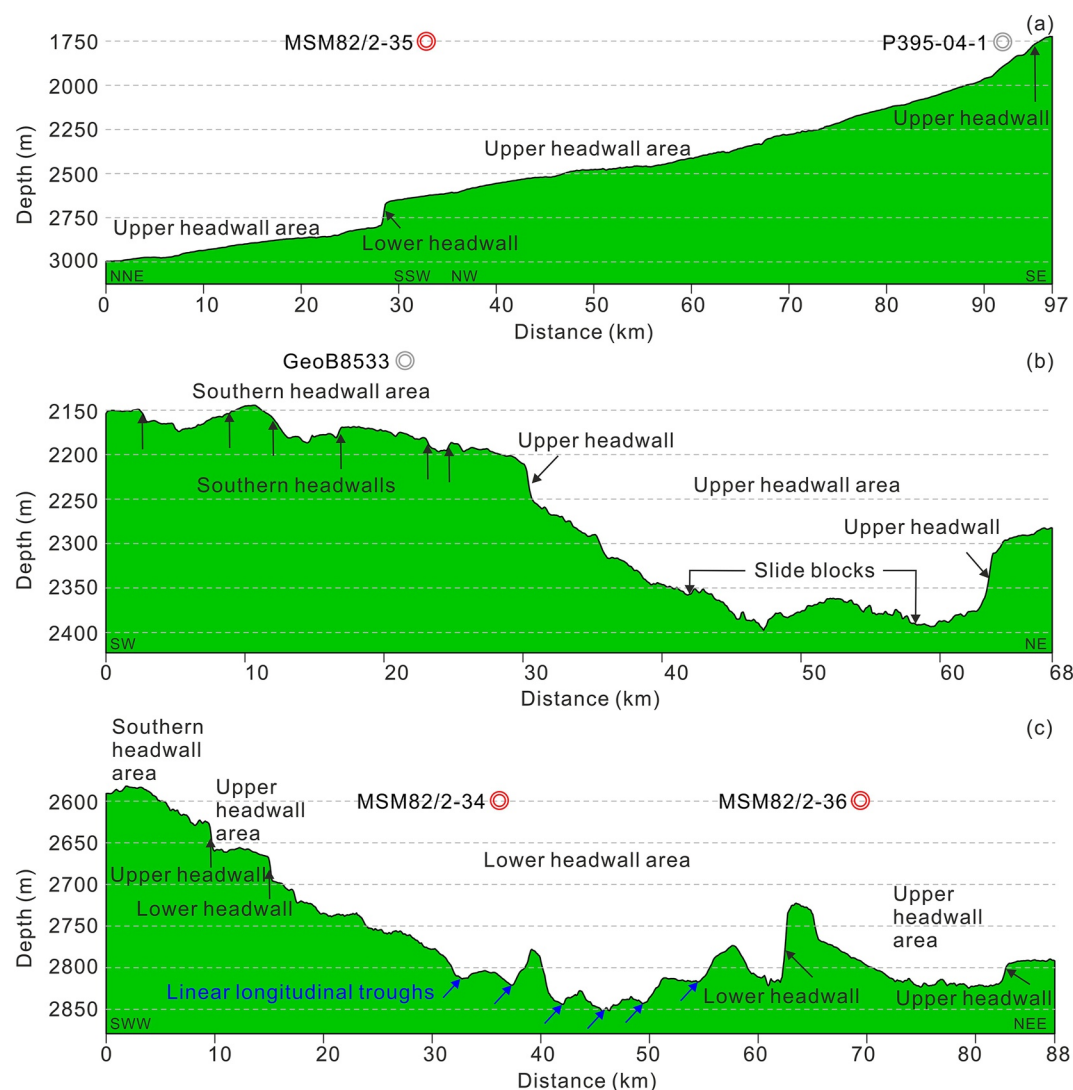


Figure 4. Morphological profiles across the different headwall areas (see Figure 2b for location). (a) seafloor depth in the upper and lower headwall areas including the locations of gravity cores P395-04-1 and MSM82/2-35. (b) seafloor depth across the upper and southern headwall including the slide blocks which are found in the central part of the upper headwall area. (c) seafloor depth across the three headwall areas. Distinct longitudinal troughs are found in the lower headwall area. Gravity cores MSM82/2-34 and MSM82/2-36 are located in the lower and upper headwall area, respectively.

continuous headwall compared to the multiple minor headwalls of the upper and southern headwall. Its height varies from 20 to 120 m with a decreasing trend downslope (Figures 2b, 4a, and 4c). The lower headwall is characterized by slope gradients between 4 and 21°, while the enclosed lower headwall area slopes only at about 0.3° (Figure 2c). The minimum size of the lower headwall area, that is, the size of the region in Figure 2d is ~5,800 km², and the lower headwall area gradually widens in downslope direction (Figure 2d).

4.2. Morphology and Structure of the Slide Deposits

We documented three main acoustic facies in the sub-bottom profile data from the working area (Table 3, Figures 5, 6, and 7). Facies 1 (F1) shows undisturbed continuous reflections representing the layered background sediments along the NW African continental margin (Table 3, Figures 5a and 7a). The slide deposits in the headwall area of the Sahara Slide Complex induce chaotic to transparent seismic reflections, and we classified them as acoustic facies 2 and 3 (Table 3, Figures 5, 6, and 7a). Facies 2 (F2) displays a chaotic to transparent pattern on top of continuous strong reflectors which most likely represent the glide planes and underlying undisturbed

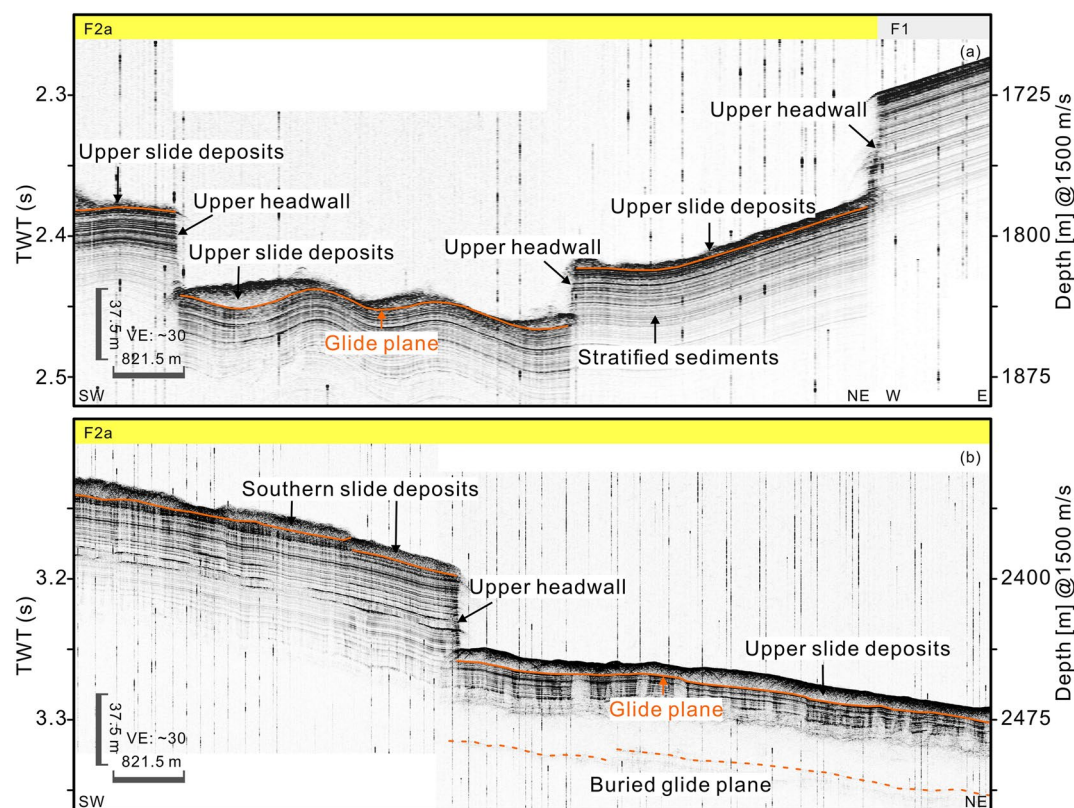


Figure 5. Sub-bottom profiles from the upper and southern headwall areas (see Figure 2b for location). The orange solid lines mark various glide planes, and the orange dashed lines show buried glide planes. (a) profile from the upper headwall area and adjacent undisturbed sediments. Horizontal color bar marks the distribution of acoustic facies F2a and F1. (b) profile crossing the upper and southern headwall area is covered by acoustic facies F2a.

sediments. Facies 2 divides into two sub-facies (Table 3): Facies 2a (F2a) shows a medium rough surface with side echoes of small blocks (Figure 5). Facies 2b (F2b) shows a hummocky seafloor of irregular hyperbolae with large blocks (up to 45 m high and 500 m wide) (Figure 6a); Facies 3 (F3) in contrast, is represented by vertically stacked chaotic reflections that also include some transparent units, and no continuous reflections are resolved beneath facies 3 (Table 3 and Figure 6b).

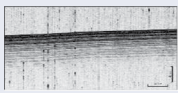
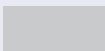
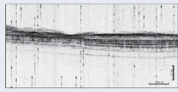

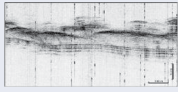
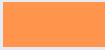
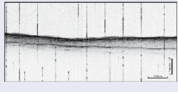

Slide deposits within the upper headwall area are characterized by the two subgroups of acoustic facies 2 (Table 3 and Figure 7a). Facies 2a covers the majority of the upper headwall area with a medium to rough seafloor. Facies 2b concentrates in the central part of the upper headwall area and includes multiple large slide blocks. The size

Table 2
Summary of Morphological Parameters From the Headwall Area of the Sahara Slide Complex

Name	Headwall			Headwall area			Slide deposit	Disturbed material
	Water depth (m)	Height (m)	Gradient (°)	Gradient (°)	Width (km)	Area (km ²)	Thickness (m)	Volume (km ³)
Upper headwall area	1650–3052	20–100 (80)	4–21	0.8	≥30	3227	1.5–43.5 (15)	177
Southern headwall area	1640–2770	5–30 (10)	2–8	0.7	≥5	2626	1.5–15 (7)	>32
Lower headwall area	2582–3118	20–120 (90)	4–21	0.3	≥43	5784	≥30	>434

Note. The number in brackets represents the mean value of related headwall's height and slide deposits' thickness, which is used for the estimation of failed materials in the headwall area of the Sahara Slide Complex. These data cover the upper headwall area, the lower headwall area, and the newly identified southern headwall area (see morphological features in Table 2 and Figure 2). The estimated volume represents the mean height of the headwall derived from bathymetric data plus the thickness of the slide deposits as seen in the sub-bottom profiles (Figure 3). For example, the average height of the upper headwall is 80 m and the slide deposit thickness in the upper headwall area is 15 m. Consequently, the estimated volume is about 177 km³ accounting for an area of 3,227 km². For the southern and the lower headwall area we can only give minimum volume estimates due to the lack of acoustic data in the distal regions.

Table 3
Acoustic Facies in the Headwall Area of Sahara Slide Complex

Acoustic facies	Filling color	Type	Location	Seismic reflection feature	Geological setting
		F1	The major part of F1 is found in the east and south of the headwall areas, minor part is located in the west among three headwall areas.	F1 shows visible and continuous bottom echoes, parallel sub-bottom reflections, low backscatter strength with few variation.	F1 represents hemipelagic deposits along northwestern African continental slope (background sediments).
		F2a	F2a is found in the entire southern headwall area, most upper headwall area and proximal part of the lower headwall.	F2a displays chaotic to transparent bottom acoustic echoes with medium rough surface above continuous reflectors, small side echoes on the rough surface, and medium backscatter strength with few variation.	F2a represents slide deposits with a few small blocks on medium rough seafloor in the whole headwall area of the Sahara Slide Complex.
		F2b	F2b is found in the middle part of the upper headwall area.	F2b presents distinct hummocky seafloor with irregular hyperbolae, acoustic spikes and high backscatter strength. A transparent sedimentary body directly beneath the seafloor lies above continuous reflectors. Some small transparent areas are embedded in the lower well stratified reflection package.	F2b represents slide deposits above undisturbed sediments with different sizes of slide blocks (up to 45 m high).
		F3	F3 is found in the lower headwall area.	F3 shows overlapping and singular hyperbolic bottom echoes with similar vertex and high backscatter strength with some variations. The hummocky features are observed within transparent sub-bottom reflections, creating stacked chaotic or transparent reflection units.	F3 represents vertically stacked slide deposits.

Note. The spatial distribution of the acoustic facies is shown in Figure 7a.

of the upper headwall area is $\sim 3,200 \text{ km}^2$, and the average thickness of the slide deposits is $\sim 15 \text{ m}$ (Table 2 and Figure 2d). We estimate the volume of failed material to $\sim 180 \text{ km}^3$ (Table 2) based on the evacuated space and the volume of slide deposits within the headwall area following the method outlined in Figure 3.

In the southern headwall area, the slide deposits form a relatively smooth seafloor with little to no slide blocks compared to the seafloor in the upper headwall area (Table 3, Figures 2d, 5b, and 7a). Acoustic facies 2a covers the entire southern headwall area with a medium rough seafloor (Figure 7a). The thickness of the slide deposits varies from 1.5 to 15 m with an average of 7 m (Table 2 and Figure 5b). We estimated a minimum volume of 30 km^3 for the disturbed deposits in the southern headwall area covered by our data (Table 2 and Figure 2d).

The slide deposits in the lower headwall area consist of facies 2a and facies 3 (Table 3 and Figure 7a). Facies 2a only covers two small patches near the lower headwall while facies 3 dominates most of the lower headwall area. Slide deposits within facies 3 in the lower headwall area are thicker than 30 m (Table 2 and Figure 6b). As the bathymetric data only cover a part of the lower headwall area we are only able to derive a minimum volume estimate of $\sim 430 \text{ km}^3$ for the failed material in the lower headwall area.

The accumulative volume of the failed material related to the Sahara Slide Complex sums up more than 600 km^3 , and as mentioned above, the real volume is much larger as major parts of the southern and lower headwall area are not yet covered with multibeam bathymetric and sub-bottom profile data. On a first view, this number seems to match with previous volume estimates between 600 and $1,100 \text{ km}^3$ (Embley, 1976, 1982; Embley & Jacobi, 1977) for the total volume of the slide complex. However, as we only derive the volume for the parts of the slide covered with shipborne bathymetric data, it needs to be stressed that the total volume (including the unmapped regions) will likely exceed $1,100 \text{ km}^3$.

4.3. Downslope Trending Continuous Linear Longitudinal Troughs

Downslope trending continuous linear topographic depressions, which can be recognized on the seafloor aspect map, are found within the entire headwall area of the Sahara Slide Complex. Their length varies between a few

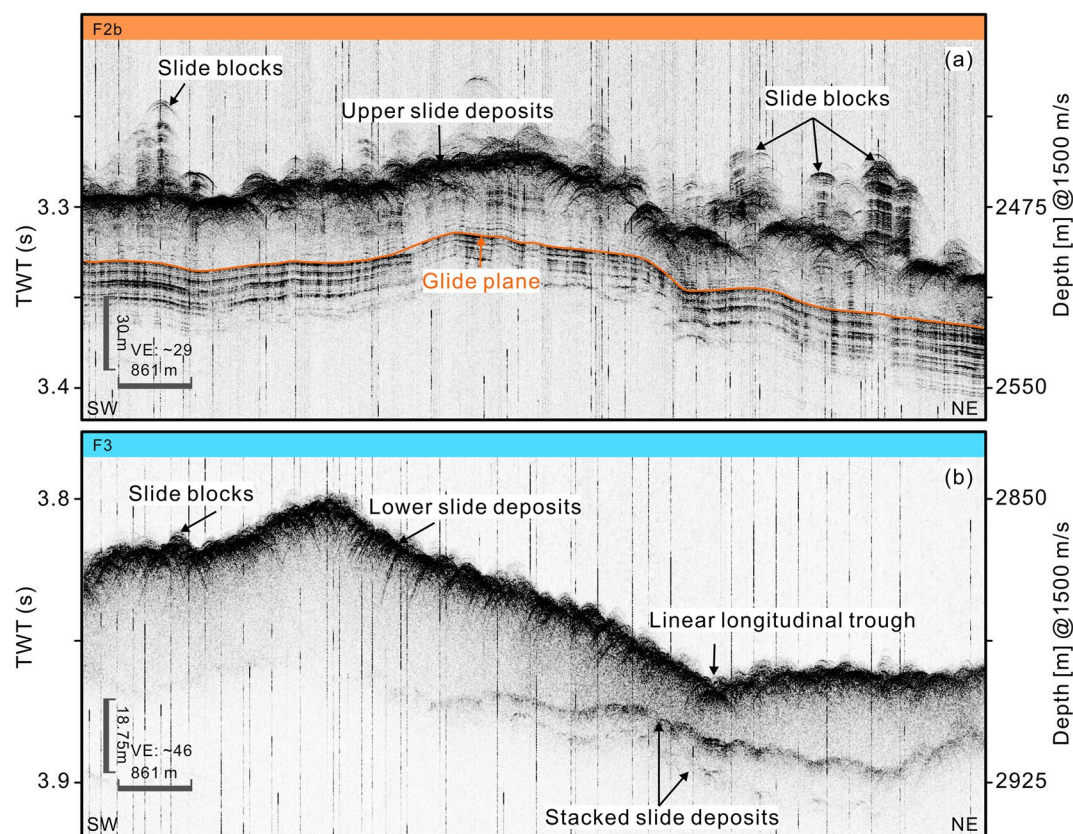


Figure 6. Sub-bottom profiles from the upper and lower headwall areas (see Figure 2b for location). (a) the profile highlights the prominent hummocky topography (acoustic facies F2b), which is characteristic for slide deposits including large slide blocks in the upper headwall area. The glide plane is marked by the orange solid line parallel to stratified sediments below. (b) profile images stacked slide deposits in the lower headwall area (acoustic facies F3), which is featured by small slide blocks and downslope trending linear longitudinal troughs.

kilometers to tens of kilometers (Figure 7b) and we refer to them as linear longitudinal troughs. Most of them start within the headwall areas and trend downslope across different headwalls (Figure 7b). Specifically, linear longitudinal troughs from the southern headwall area continue into the upper headwall area, whereas those that originate in the upper headwall area can be traced into the lower headwall area. The lower headwall area holds intervening downslope trending topographic highs (ridge-like) between linear longitudinal troughs. They are well developed and up to 35 m high and 35 km long (Figures 4c, 6b, and 7b). Linear longitudinal troughs show a V-shaped cross profile with various widths from hundreds to thousands of meters, and depth between 0.5 and 13 m (Figure 4c).

4.4. Sedimentological Observations and Dating of Gravity Cores

Gravity cores GeoB8532 and GeoB8533 sampled the uppermost 5.17 m (GeoB8532) and 5.04 m (GeoB8533) of the shallow sediments within the upper and southern headwall area, respectively (Table 4 and Figure 2c). Core GeoB8532 retrieved about 13 cm of hemipelagic sediment above a blocky slide debris (Figure 8). The debris layer comprises abundant clasts, sharp irregular contacts and sheared boundaries (Georgiopolou et al., 2009). Core GeoB8533 from the southern headwall area also contains hemipelagic olive-green mud at the top (~10 cm thick) above slide deposit (Georgiopolou et al., 2010; H. D. Schulz & Hanebuth, 2003). A density peak at 10 cm, which vanishes in upward direction, further confirms the boundary between hemipelagic sediment and slide deposits (Figure 8) (Georgiopolou et al., 2010). Two additional gravity cores (P395-04-1 and P395-07-1) from RV Poseidon cruise P395 sampled the shallow failed and deformed sediments just beneath the upper headwall (Table 4 and Figure 2c). Li et al. (2017) dated one clast of the debrite deposits in core P395-04-1 to $6,172 \pm 78$ years BP. The maximum age of the undisturbed shallow hemipelagic drape (~4 cm) within core

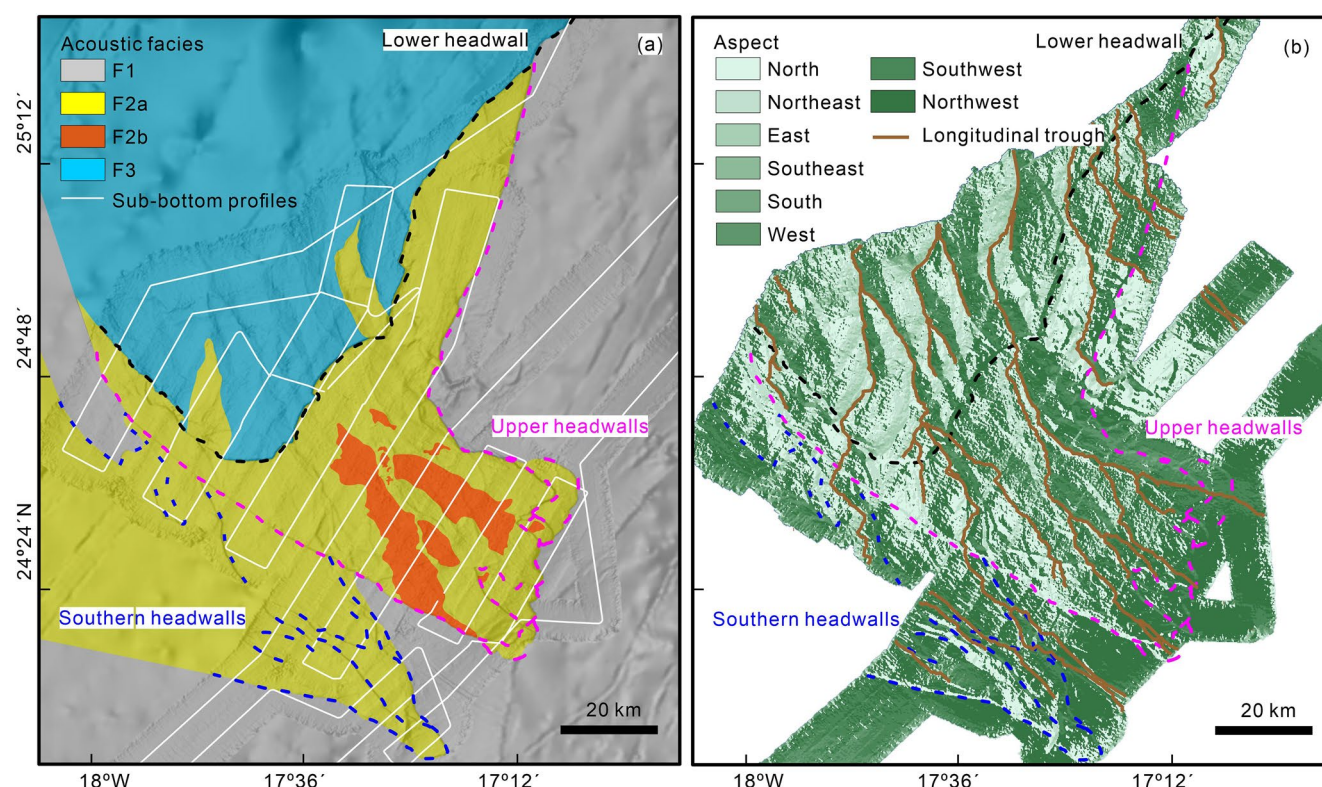


Figure 7. Shaded relief map highlighting structural features from the headwall area of the Sahara Slide Complex: (a) spatial distribution of acoustic facies in the headwall area. The white solid lines provide the survey lines for sub-bottom profiles and bathymetric data. Bathymetric data filling surrounding gaps is from the GEBCO2020 grid (GEBCO Compilation Group, 2020). Compare Table 3 for details. (b) aspect map of the headwall area highlighting the downslope trending continuous topographic features, where longitudinal troughs are marked by brown solid lines.

P395-07-1, that overlies deformed and redeposited material, was estimated to $1,840 \pm 23$ years BP (Figure 8) (Li et al., 2017).

Three additional gravity cores from the headwall area were taken during RV Maria S. Merian cruise MSM82/2 in 2019 (Krastel, Barrett, et al., 2019). From these, core MSM82/2-34 locates in the lower headwall area whereas cores MSM82/2-35 and MSM82/2-36 sample the sediments within the upper headwall area (Table 4 and

Table 4
Gravity Cores From the Headwall Area of the Sahara Slide Complex, Including Location, Water Depth, Recovery Length, Age of Dated Samples From Gravity Cores, and Failure Timing

Station	Latitude	Longitude	Depth (m)	Recovery (m)	Dated sample position (cm)/bsf	Dated sample age (yr)/BP	Failure timing/yr
GeoB8532	24°25.50'	−17°11.51'	2125	5.17	/	/	2,600
GeoB8533	24°16.71'	−17°32.00'	2184	5.04	/	/	2,000
P395-04-1	24°14.70'	−17°14.70'	1930	2.57	5	$6,172 \pm 78$	$6,172 \pm 78$
P395-07-1	24°27.36'	−17°08.18'	2132	4.8	3	$1,840 \pm 23$	$2,240 \pm 200$
MSM82/2-34	24°43.77'	−17°40.06'	2811	4.37	2–3	$9,212 \pm 72$	$9,212 \pm 500$
MSM82/2-35	24°41.89'	−17°33.56'	2631	4.35	3–4	$5,978 \pm 57$	$5,978 \pm 500$
MSM82/2-36	24°53.16'	−17°23.20'	2790	4.33	4–5	$13,486 \pm 69$	$13,486 \pm 500$

Note. Cores GeoB8532, P395-04-1, P395-07-1, MSM82/2-35 and MSM82/2-36 are located in the upper headwall area, core GeoB8533 in the southern headwall area, and core MSM82/2-34 in the lower headwall area (see location in Figure 2c). Information on cores GeoB8532 and GeoB8533 are from Georgiopolou et al. (2009) and Georgiopolou et al. (2010) respectively, and information on cores P395-04-1 and P395-07-1 are from Li et al. (2017).

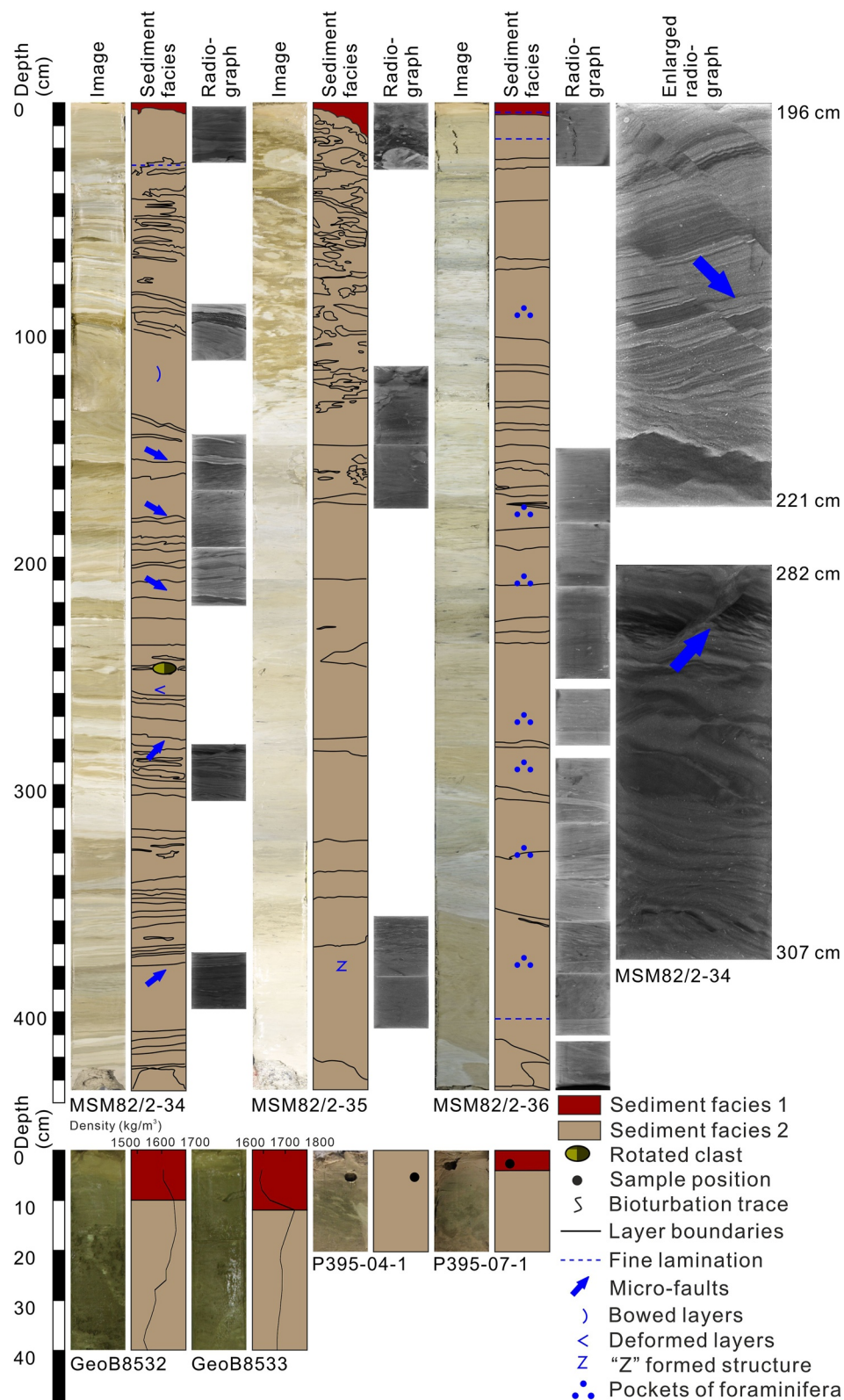


Figure 8. Image, sediment facies and radiography of gravity cores GeoB8532, GeoB8533, P395-04-1, P395-07-1, MSM82/2-34, MSM82/2-35 and MSM82/2-36 (see Figure 2c for location). Core GeoB8532 and GeoB8533 are from Georgiopolou et al. (2009) and Georgiopolou et al. (2010) respectively. Core P395-04-1 and P395-07-1 are from Li et al. (2017). Black dots show the position of dated samples. Sediment facies 1 (SF1) marked in red represents top hemipelagic sediments, and sediment facies 2 (SF2) in brown color indicates the disturbed slide deposits below.

Figure 2c). The sedimentological characteristics and dating of these cores help to shed further light on the chronological sequence of various slide events within the headwall area of the Sahara Slide Complex.

All three cores separate into two distinct sedimentary sections, which we refer to as sediment facies 1 (SF1) and sediment facies 2 (SF2) (Figure 8). SF1 corresponds to post-slide sediments which reach a thickness of 0–4 cm (MSM82/2-34), 0–4.5 cm (MSM82/2-35), and 0–6.5 cm (MSM82/2-36). It contains reddish-brown sediments consisting of silt and clay which are partly influenced by bioturbation (Figure 8). SF1 appears homogenous without visible structures in cores MSM82/2-34 and MSM82/2-35, but includes very fine laminations in core MSM82/2-36 (Figure 8). The underlying SF2 consists of disturbed slide deposits (4/6.5–433/437 cm). The color of SF2 changes to brown with some gray variations (Figure 8). The dominant sediment types in SF2 are silt and clay, but fine sand grains and clasts are also visible. Sediment facies 2 in core MSM82/2-34 starts with a wavy, non-parallel bedding that is slightly tilted from 60 to 100 cm core depth (Figure 8). The deformed laminations show staircase-like features that merge into curved layers between 110 and 140 cm core depth. Micro-faults with different faulting directions are found underneath the prevailing deformation structures (Figure 8). The different layers range from bright (white to yellow-brownish) to dark (brown-greyish to brownish) colors (Figure 8). Within core MSM82/2-35, the size of clasts varies from 1 to 12 cm between 9 and 165 cm core depth, with an overall decrease down the core (Figure 8). This leads to a discontinuous, wavy, non-parallel bedding. Additionally, staircase-like structures occur as directed deformation features. The sections below 165 cm of core MSM82/2-35 change to a discontinuous, curved, non-parallel bedding including scattered patches of brighter (white to yellow-brownish) or darker (brownish) colors (Figure 8). The thickness of the layer packages varies between few centimeters and up to ~50 cm, including the partly deformed chaotic layers (e.g., 360–380 cm core depth). Sediments facies 2 in the core MSM82/2-36 shows only slightly wavy or tilted laminations between 7 and 290 cm core depth (Figure 8). Below this, the deformed curve-layers extend until the base of 435 cm core depth. The deformation of the sediments can be seen very clearly especially between 405 and 435 cm (Figure 8). Sediment colors change throughout the entire core from white greyish to brown-greyish and brown (Figure 8). Pockets filled with foraminifera are found between 80 and 390 cm core depth.

Foraminifera (*Globigerinoides ruber*) samples from the top unit (SF1) of all three gravity cores collected at cruise MSM82/2 are used for dating of the shallow hemipelagic sediments covering the slide deposits. Samples were taken directly above the boundary to SF2 at depths of 2–3 cm (MSM82/2-34), 3–4 cm (MSM82/2-35), and 4–5 cm (MSM82/2-36) (Figure 8). The obtained ages correspond to $9,212 \pm 72$ years BP in the lower headwall area (MSM82/2-34), and at $5,978 \pm 57$ years BP (MSM82/2-35) and $13,486 \pm 69$ years BP (MSM82/2-36) in the upper headwall area (Table 4, Figures 2c and 8). However, all extracted samples for dating in SF1 are in the range of bioturbation, which might complicate a precise age determination. Therefore, the obtained ages cannot be treated as definite age for the slope failure, but rather give a minimum age for the hemipelagic sediments above the slide deposits. From these ages, we calculated the age of the slide event in each core based on a background sedimentation rate and the vertical distance of the dated sample above the top of the slide deposits.

Gravity core M12392-1 of RV Meteor cruise M25 sampled hemipelagic sediments from the continental slope to the east of the Sahara Slide Complex (Figure 1). It provides a sedimentation rate of ~5 cm/kyr between the seafloor and a sub-bottom depth of ~70 cm (Müller & Suess, 1979). We use this sedimentation rate to estimate the time needed for the deposition of the sediments between the top of the slide and the dated sample (thickness: 1.5 cm in core MSM82/2-34, 1.0 cm in core MSM82/2-35 and 2.0 cm in core MSM82/2-36). The ages of the individual landslides correspond to $9,212 \pm 500$ years (MSM82/2-34), $5,978 \pm 500$ years (MSM82/2-35), and $13,486 \pm 500$ years (MSM82/2-36) (Table 4). The error in these age estimates range around ± 500 years considering the combined effect of the dating error, uncertainties in the sedimentation rate, and the determination of the upper boundary of the slide deposits.

5. Discussion

The Sahara Slide Complex represents one of the largest seafloor morphological features along the NW African continental margin with an affected area of about 50,000 km² (Embley, 1982; Gee et al., 1999; Georgiopolou et al., 2010; Masson et al., 1993). After its discovery in the seventies, it has been regarded as a single failure event that occurred around 60 kyr (Embley, 1976; Gee et al., 1999). Georgiopolou et al. (2010) described two ~100 m-high headwall scarps and suggested a series of multiple slide events. However, a detailed description and

reconstruction of the individual events was not possible due to the lack of multibeam bathymetric and sedimentological data. After collection of additional multibeam bathymetric data, sub-bottom profiles, side-scan sonar data and sediment cores, Li et al. (2017) provided further evidence for multiple individual headwalls including the lower headwall located in water depth >2700 m. Knowledge on the lower headwall was, however, mainly based on a single swath transect extending into deeper water (Figure 2 in Li et al. (2017)). The here presented new high-resolution multibeam bathymetric data and sub-bottom profiles in concert with new and legacy sediment cores allow, for the first time, to put the upper and the lower headwall in context. We further document evidence for an additional southern headwall. Together, the new data reveal a complex structure and morphology of the Sahara Slide Complex that systematically changes throughout the headwall area, and that can hardly be explained with a single failure event.

5.1. Morphology and Structure of the Headwall Areas of Sahara Slide Complex

Linear longitudinal troughs that extend across different headwalls dominate the seafloor morphology in the headwall area on a large scale. Sedimentary furrows also display linear characters in estuaries, large lakes and on the seafloor. Flood (1983) proposed that the branching patterns of sedimentary furrows can be developed in abyssal calcareous oozes (Samoan Passage, Saharan Rise). As for the linear longitudinal troughs in the hemipelagic setting of the Sahara Slide headwall areas, we interpret them as the result of erosional processes induced by failure of more proximal sections of the Sahara Slide Complex. While traveling downslope, slide debris from the upper and southern headwall area likely gets funneled through these depressions, thereby causing a widening and deepening of the troughs. Hence, we infer that the lower headwall formed first and that subsequent failures of the upper and southern headwall mobilized the materials that led to the formation of the linear longitudinal troughs in the whole headwall area and associated linear longitudinal ridges in the lower headwall area of the Sahara Slide Complex.

Acoustic facies F2, with its distinct two-unit pattern including shallow slide deposits and stratified sediments below, dominates the upper headwall area (Table 3, Figures 5, 6a, and 7a). Facies F2 is divided into sub-facies F2a and F2b with medium and rough to smooth seafloor, respectively. Facies F2a covers most part of the upper headwall area, which consists of the typical slide deposits of clastic debrites (Figures 5 and 7a). Facies 2b represents slide blocks that concentrate in the central part of the upper headwall area (Figures 6a and 7a). All glide planes in the upper headwall area trend parallel to the undisturbed stratified sediments below (Figure 5), which implies apparent bedding-plane failures by translational sliding. We also found indications for several older buried glide planes in the upper headwall area (Figure 5b), which indicates a long history of an unstable slope.

The entire southern headwall area is covered by acoustic facies F2a (Table 3, Figures 5b and 7a). Glide planes in the southern headwall area also trend parallel to the stratified sediments below, which again implies mass movement by multiple translational slides. Similar morphologies with multiple escarpments and bedding parallel glide planes have been reported, among others, for the Nyk slide, the Storegga slide, and multiple smaller mass movements offshore the Lofoten Islands (Baeten et al., 2014; Bryn et al., 2005; Haflidason et al., 2005; Lindberg et al., 2004).

The lower headwall area displays one single well-developed headwall, in contrast to the upper and southern headwall areas which have multiple headwalls (Figures 2b and 2c). Furthermore, no big slide blocks are found in the lower headwall area (Figures 2b, 4c, and 6b). Stacked slide deposits without stratified sediments below (acoustic facies F3) dominate the lower headwall area (Table 3, Figures 6b and 7a). Farther southwards along the NW African continental margin, the Mauritania Slide shows a similar pattern of stacked slide deposits that are interpreted to result from a series of individual slide events (Henrich et al., 2008). The stacked slide deposits and the above-mentioned downslope trending continuous linear longitudinal troughs support the interpretation that the lower headwall formed before the upper and the southern headwall. In the following section we further explore the timing of the different slide events based on morphological considerations, published sediment core data and new age dating of gravity cores presented in this study.

5.2. Sequence of Failure Events Within the Headwall Areas of Sahara Slide Complex

Georgiopolou et al. (2007) proposed that most of the buried and stacked slide events in the upper headwall area of the Sahara Slide Complex developed as retrogressive slides. The Storegga Slide is a prime example for

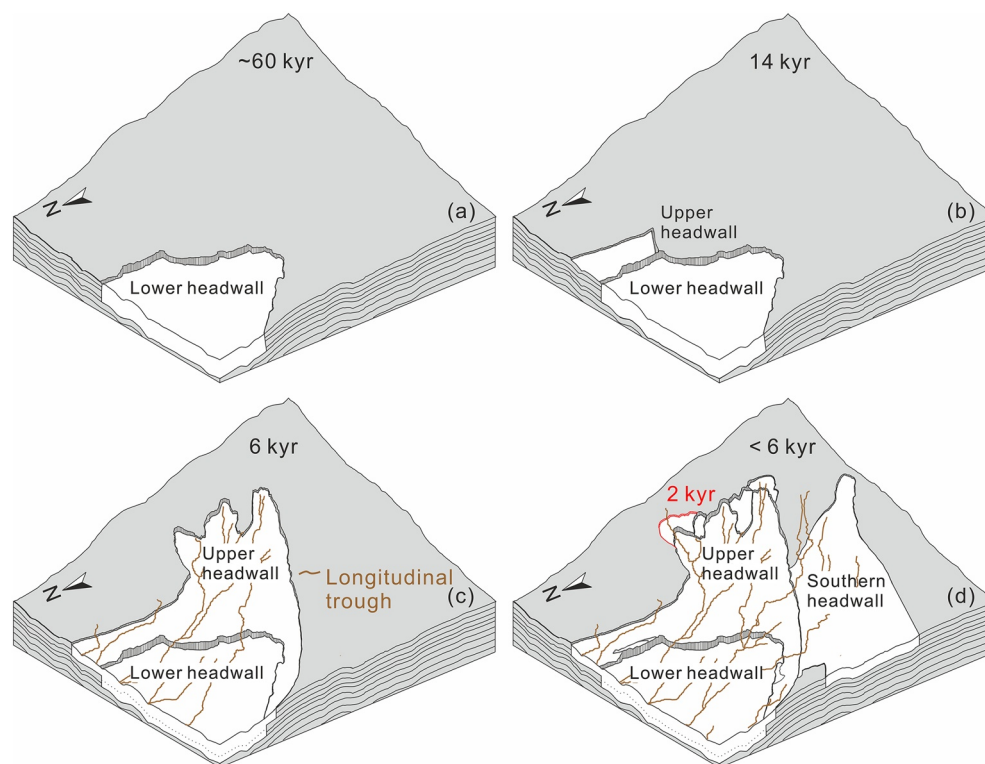


Figure 9. Conceptual model of the sequence of slide events that shaped the headwall area of Sahara Slide Complex from 60 to 2 kyr. The lower headwall failed at 60 kyr (a); which was followed by a failure of the northeastern part of upper headwall at ~14 kyr (b); a major slope failure in upper headwall area occurred at 6 kyr (c); slide events in the upper and southern headwall area happened after 6 kyr (d).

a sequence of translational slides that retrogressively developed in upslope and lateral direction. This induced typical grabens and ridges parallel to the headwall (Kvalstad et al., 2005). From our updated bathymetric compilation, we do not observe distinct graben and ridge structures between the upper and the lower headwall, which would support the formation of these two headwalls by a retrogressive failure (Zhang et al., 2021). Retrogressive rotational slumps around the epicenter of the 1929 Grand Banks earthquake are, for example, spaced at distances between 7 and 20 km (Piper et al., 1999). Furthermore, a series of large and slightly inclined terraces form individual headwalls of the Storegga Slide scar are spaced at a distance between 5 and 10 km (Kvalstad et al., 2005). The large distance (~55 km) between the upper and lower headwall of the Sahara Slide Complex appears unusual for a typical retrogressive failure. In addition, the long time gap between the individual events (~60 kyr for the lower headwall and ≤ 6 kyr for the main failure of the upper headwall, see below) does not match with typical retrogressive slides. We therefore consider the failure of the lower and the upper headwall as individual slide events. However, we cannot exclude that the Sahara Slide Complex might be an end-member of a large retrogressive slide with a long temporal and spatial gap between the formation of individual headwalls. The morphologies of the upper and southern headwall as well as the setting of several buried slides, however, suggest a formation of most of the individual headwall areas of the Sahara Slide Complex by retrogressive failures, as already suggested by Georgiopolou et al. (2007).

Masson et al. (2002) showed that slide deposits can be used to reconstruct flow types and sliding processes, and that the dating of sediments that drape such slide deposits can help to constrain the ages of slides. Coccolith assemblages from the distal part of Sahara Slide indicate that emplacement occurred close to marine oxygen-isotope stage 3/4 (around 60 kyr) (Gee et al., 1999). A failure of the lower headwall at around ~60 kyr (Figure 9a) would correlate to a rapid sea level rise after a significant sea level lowstand (boundary between MIS4 and MIS3; Shackleton et al. (2000)) (Figure 10). Sediment core MSM82/2-34 taken in the lower headwall area holds internal deformation structures: thinning, stretching, shearing, and one rotational fold of debrites (Figures 2c and 8). The reconstructed age of 9 kyr for the slide deposits of core MSM82/2-34 suggests that they do not relate to the 60 kyr

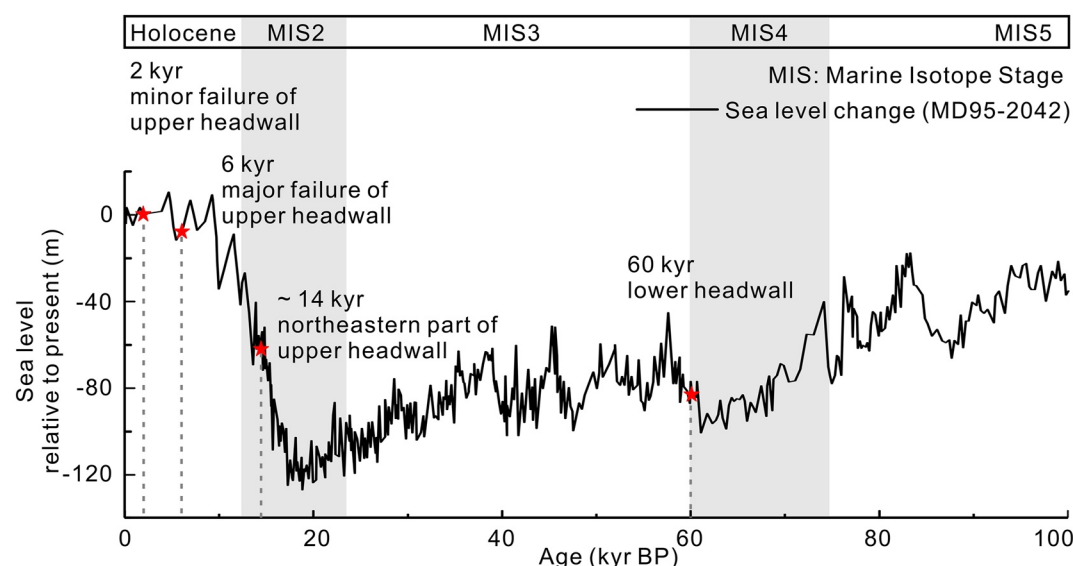


Figure 10. Timing of slope failures within the Sahara Slide Complex (red stars) shown on top of sea level changes for the North Atlantic Ocean during the last 100 kyr (Shackleton et al., 2000). MIS = Marine Isotope Stage. MIS2 and MIS4 correspond to glacial intervals, while MIS3 and MIS5 are interglacial periods.

failure of the lower headwall. Instead, the slide sediments of this core originate from a Holocene failure within the upper headwall area or the southern headwall area. We want to point out that the assumption of a constant sedimentation rate is only a first approximation and we cannot exclude that the undisturbed hemipelagic sediments in core MSM82/2-34 are overprinted by gravitational derived material from farther upslope. In any case, it is not possible to relate the ~9 kyr age to a distinct failure within the whole headwall area, and more dated sediment samples from the slide deposits are necessary to better constrain the timing of individual slide events.

Based on the dated age of Holocene hemipelagic sediments in core MSM82/2-36 and average sedimentation rate, the associated failure timing is ~14 kyr in the northeastern part of the upper headwall area. Embley (1982) reported an age of $15,325 \pm 475$ years BP for a sample from a hemipelagic drape (15–19.5 cm) of piston core V32-42, which was retrieved in the depositional zone of the Sahara Slide Complex (Figure 1). A turbidite channel is located slightly to the south of core MSM82/2-36 (Figure 2b). The sedimentary record of this core might be influenced by turbidites from this channel. High relief on the seafloor to the south of the turbidite channel may prevent the deposition of slide material from the more southern part of the upper headwall area (Figure 2b). Consequently, the slide sediments in core MSM82/2-36 and the distal V32-42 might have originated in the northeastern part of the upper headwall area at ~14 kyr (Figure 9b). Younger slide events of ~6 kyr are found in cores MSM82/2-35 and core P395-04-1 (Li et al., 2017) in the central and uppermost part of the upper headwall area, respectively. They indicate that at least one major slide event occurred at ~6 kyr in the upper headwall area (Figure 9c).

Around 13 cm of in-situ hemipelagic sediments overly the blocky debris layer in core GeoB8532 (Georgiopoulou et al., 2009) (Figures 2c and 8), where the estimated age of the failure is ~2.6 kyr. Li et al. (2017) provided an age ~2 kyr for a slope failure in the most proximal part of the upper headwall area (core P395-07-1 in Figure 2c). About 10 cm of hemipelagic olive-green mud in the shallow most section of gravity core GeoB8533 (Georgiopoulou et al., 2010) (Figures 2c and 8) indicate that the underlying failed sediment was deposited at 2 kyr in the southern headwall area based on an average sedimentation rate of 5 cm/kyr (Müller & Suess, 1979). The downslope trending continuous linear longitudinal troughs crossing different headwalls imply that the multiple slide failures in southern headwall area should be younger than the major event at 6 kyr forming the upper headwall area, but the order of multiple slides is still unclear in the southern headwall area (Figure 9d).

The headwall area of Sahara Slide Complex was affected by multiple individual slope failure events between 60 and 2 kyr (Figure 9). This indicates a long failure history of the NW African continental margin. Although our age estimates include a high degree of uncertainty with respect to the possible dating errors, assumed constant

sedimentation rates, the exact determination of the upper boundary of slide deposits, and the relationship of slide deposits among individual headwall failures, we are able to derive a relative sequence of failure events (Figure 9): at around 60 kyr, the lower headwall failed and some slide deposits were deposited within the lower headwall area; then the northeastern part of upper headwall followed at ~ 14 kyr; at about 6 kyr the major part of the upper headwall area was formed, and the mobilized sediments overprinted the slide deposits from the failure of lower headwall; after 6 kyr multiple smaller slides occurred in the proximal part of the upper headwall area and within the whole southern headwall area; the youngest documented failure event occurred at 2 kyr in the northeastern proximal part of the upper headwall area.

5.3. Preconditioning Factor and Implications for Geohazard

Scarselli (2020) summarized pre-conditioning and triggering factors for submarine landslides. They include slope steepening, seismic shaking, wave loading and excess pore fluid pressure. The slope gradient in the area of the Sahara Slide headwall is less than 3° , which makes slope steepening an unlikely pre-conditioning factor for the failure. Earthquakes are rare along the passive NW African continental margin, although moderate magnitude events ($4 \leq M \leq 6$) are sometimes recorded. No recent major earthquakes ($M > 6$) affected the region of the Sahara Slide Complex, while there were some small events at the adjacent volcanic Canary Archipelago (Earthquake Catalog since 1959 from USGS: <https://earthquake.usgs.gov/earthquakes/search/>). Wave loading includes different kinds of water movements which could initiate slope failures. Sea level changes might be a crucial factor, which is controversially discussed (e.g., Lee, 2009; Li et al., 2017; Urlaub et al., 2013). Urlaub et al. (2013) stated that there is no clear correlation of landslide frequency with sea level change. We also did not find a clear correlation between the failure timing of the Sahara Slide Complex and sea level change (Figure 10). Multiple factors can cause excess pore fluid pressure including dissociation of gas hydrates, fluid migration, and high sedimentation rate. No indications for gas hydrates or fluid migration and seafloor seepage are found in the data. Sedimentation rates are normal in the failure area (~ 5 cm/kyr) as determined in Core M12392-1 located ~ 70 km north of the headwall area of the Sahara Slide Complex (Müller & Suess, 1979). Modeling results suggest that sedimentation rates in this range are insufficient to destabilize the slope (Urlaub et al., 2015).

Bottom-currents may also precondition slope stability, as they can cause toe-erosion or they build contourites, which are known to be prone to failure (Laberg & Camerlenghi, 2008). Hydrographic and oceanographic data of the NW African continental margin show that it is affected by a complex composition of water masses, including South Atlantic Central Water, North Atlantic Central Water, Mediterranean Water, Antarctic Intermediate Water, and North Atlantic Deep Water (Hagen, 2001). From these, the North Atlantic Deep Water is the dominating current in the headwall area of the Sahara Slide Complex (1,500–4,000 m of water depth) (Sarnthein et al., 1982). Sediment waves and other current induced sedimentary features are found along the NW African continental margin at many places (Wynn et al., 2000), but we do not recognize any of these features which may contribute to the destabilization of the slope in our data around the headwall area of the Sahara Slide Complex.

Sediments with lower strength compared to their adjacent units can initiate submarine mass movements at micro triggering conditions (Locat et al., 2014). Such weak layers are considered as one of the most important preconditioning factors for submarine landsliding (Gatter et al., 2021; Locat et al., 2014), such as the Storegga Slide (Kvalstad et al., 2005), and the Nice airport failure (Dan et al., 2007). For the Sahara Slide Complex, all glide planes, including the buried ones, trend parallel to the undisturbed stratified sediments (Figures 5 and 6a). This supports the presence of multiple weak layers at different stratigraphic depths that could result from recurring sedimentation patterns such as those induced by glacial-interglacial cycles. To destabilize low gradient ($<2^\circ$) continental slopes, such as along large parts of the NW African continental margin, the compressibility of the sediment plays an important role (Urlaub et al., 2015). Although the nature of weak layers differs between different geologic settings, high compressibility seems to represent a key characteristic of them. Diatom ooze layers with a high compressibility have been identified as weak layers for the Cap Blanc slide offshore northern Mauritania about 600 km to the south of the Sahara Slide Complex (Urlaub et al., 2018). Diatom oozes are also recovered at the DSDP Site 139 drilled during Leg DSDP-Leg 14 (Hayes et al., 1972), and this site is located less than 200 km southwest of the headwall area of the Sahara Slide Complex. Diatom oozes, which are common along many continental margin, may represent a preconditioning factor for global submarine mega-slides at low gradient slopes (Urlaub et al., 2018), including the Sahara Slide Complex. The pervasive presence of these glide planes suggests that the study area, and possibly large parts of the NW African continental margin, are dissected

by recurring sedimentary layers that can act as weak layers under certain circumstances. Yet we do not know why certain segments of the NW African margin have failed along a respective layer, whereas the adjacent slope remains stable despite continuity of stratigraphic layers and constant low slope gradients.

Krastel et al. (2018) stated that mega-slides along the NW African continental margin have the potential to trigger tsunamis, although no confident evidence for a tsunami caused by a landslide has been identified so far. The Sahara Slide Complex is one of these mega-slides. It is well proven that landslides of similar size as the Sahara Slide Complex triggered significant tsunamis. The 1929 Grand Banks landslide off the coast of Newfoundland caused a devastating tsunami with heights up to 13 m claiming 28 lives (Fine et al., 2005). Modeling suggest that a $>100 \text{ km}^3$ slump was responsible for the high tsunami run-ups in Newfoundland (Løvholt et al., 2018). Numerical simulations and tsunami deposits from the 8150-year BP Storegga Slide reveal tsunami run-up of 10–12 m high above sea level in western Norway, 3–6 m high in the northeast Scotland and above 20 m high on the Shetland Islands (Bondevik et al., 2005; Harbitz, 1992). The Grand Banks and Storegga landslide tsunamis are two of only few documented examples where landslide-generated tsunamis may be observed at transoceanic distances. Landslide-generated tsunamis are usually highly dispersive. Hence, landslides may generate very large wave amplitudes locally, which then disperse rapidly (Glimsdal et al., 2013). Therefore, much smaller landslides are capable of triggering significant local tsunamis. A comprehensive review of landslide triggered tsunamis is given by Harbitz et al. (2014). A prominent example is the 1998 Papua New Guinea tsunami causing more than 2000 fatalities. It is believed that this tsunami was triggered by a 5 km^3 slump in about 1,400 m water depth (Tappin et al., 2008). Recent examples of landslide triggered tsunamis are the 2018 Palu Bay tsunami in Sulawesi and the 2018 tsunami caused by a lateral collapse of the volcano Anak Krakatau in the Sunda Straits. The observed tsunami run-ups around Palu Bay could only be reproduced by a combined earthquake and coastal landslide model (Schambach et al., 2021). The Anak Krakatau collapse generated a tsunami up to 13 m high on the adjacent coasts of Sumatra and Java (Grilli et al., 2019).

These examples show that the Sahara Slide Complex, with a minimum estimated volume of mobilized material more than 600 km^3 (Table 2) could have caused a significant tsunami. However, each individual headwall area was most likely formed by multiple failures of smaller volumes, although even smaller volumes would be sufficient for the generation of tsunamis. We want to point out that the volume of the failed mass is only one parameter controlling the tsunami potential of landslides and other parameters such as water depth, rapid initial acceleration of the failed material, style of failure, and the type of sediments involved in the failure play important roles as well (Løvholt et al., 2015; Ward, 2001). Hence, it is extremely difficult to assess the tsunami potential based on our data. Georgiopoulou et al. (2009) inferred that the 60 kyr failure of the Sahara Slide Complex was most likely a slow slide because of no related turbidite in its proximal source zone. This setting suggests a low tsunami potential. On the other hand, Georgiopoulou et al. (2009) describe turbidite deposits $\sim 700 \text{ km}$ downslope of the Sahara Slide, which they interpret to have formed by a failure of the headwall of the Sahara Slide Complex at about 2 kyr. This implies a relatively fast moving landslide body with potentially higher tsunami potential. In summary, we consider it as likely that some of the failures of the Sahara Slide Complex triggered tsunamis, but we do not have the data to assess the tsunami potential of individual failures. Definitive proof for the tsunami generation potential of the Sahara Slide Complex could only be provided by identifying tsunami deposits on the coast, but such work has not yet been done.

6. Conclusions

We provide a comprehensive view on the entire headwall area of the Sahara Slide Complex by combining new and legacy multibeam bathymetric, sub-bottom profile, and gravity core data. The complex seafloor morphology and subseafloor structure, in combination with a large range of slide ages, suggests that the headwall area was shaped by multiple slide events over at least the 60-2 kyr time period. The sequence of multiple slide events underlines the unstable nature of the continental slope in the study area and possibly along large parts of the NW African continental margin. The following detailed conclusions can be drawn:

1. The Sahara Slide Complex is formed by three major headwalls: the upper, southern and lower headwall. The related upper and southern headwall area hold multiple slide events, while the lower headwall area might be generated by one big main failure. Multiple bedding-parallel glide planes are visible in the upper and southern

- headwall area, while no stratified sediments are resolved below the slide deposits in the lower headwall area, possibly resulting from the limited penetration of the sub-bottom profile data.
- We recognized three major types of acoustic facies representing various sedimentological process and depositional settings: Facies 1 represents the undisturbed hemipelagic sediments of the NW African continental margin with silt, clay, carbonate-rich marls and oozes surrounding the headwall areas; Facies 2 stands for the two-unit pattern with slide deposits and stratified sediments below, which populated the upper and southern headwall area; Facies 3 marks vertically stacked slide deposits without visible strata beneath the lower headwall.
 - Based on seafloor morphology and dated sediment samples we derive a relative sequence of slope failures in the headwall area of the Sahara Slide Complex: the lower headwall failed at around 60 kyr, followed by a failure of the northeastern part of the upper headwall area at ~14 kyr. At 6 kyr, a major slide event occurred in the upper headwall area. Subsequently, the failure of the southern headwall area as well as several smaller slides in upper headwall area with the youngest at 2 kyr, generated the present seafloor morphology visible in the multibeam bathymetric data.
 - There is no morphologic evidence for a retrogressive sliding pattern between the upper and the lower headwall, although a retrogressive pattern cannot be ruled out based on the available data. Vertically stacked slide deposits in the lower headwall area imply that they relate to individual slide events. Failure along multiple bedding-parallel glide planes indicate that weak layers are pervasively present within the study area, and possibly along large parts of the NW African continental margin. These weak layers may be the preconditions for future slope failures.

Data Availability Statement

Access to the bathymetric data, sub-bottom profiles and gravity cores can be found in the repository of PANGAEA: Tang and Krastel (2022, <https://doi.org/10.1594/PANGAEA.943644>).

Acknowledgments

We would like to acknowledge the invaluable assistance of fellow cruises participants, the captains and crews of cruises Meteor 58/1, Poseidon 395, Maria S. Merian 11/2, 82 and 87. Q. Tang is thankful to the Ph.D. funding of China Scholarship Council. Thanks for IHS Markit (Kingdom) providing free academic license at Kiel University. We greatly acknowledge the constructive reviews of Suzanne Bull and Davide Gamboa, which helped us to improve the manuscript significantly. Open Access funding enabled and organized by Projekt DEAL.

References

- Baeten, N., Laberg, J., Vanneste, M., Forsberg, C., Kvalstad, T., Forwick, M., et al. (2014). Origin of shallow submarine mass movements and their glide planes—Sedimentological and geotechnical analyses from the continental slope off northern Norway. *Journal of Geophysical Research: Earth Surface*, 119, 2335–2360. <https://doi.org/10.1002/2013JF003068>
- Bickert, T., Braun, S., Fricke, S., Hermann, B., Just, J., Keil, H., et al. (2011). *Pre-site survey for an IODP cruise Neogene paleoclimate and sediment transport at the continental margin of NW Africa - Cruise No. MSM11/2 - March 14 - April 09, 2009 - Dakar (Senegal) - las palmas (Canary Islands, Spain)* (2195-8483). MARIA S. MERIAN-Berichte. Retrieved from https://www.tib.eu/de/suchen/id/awi%3Adoi%7E10.2312%252Fcr_msm11_2
- Bondevik, S., Løvholt, F., Harbitz, C., Mangerud, J., Dawson, A., & Inge Svendsen, J. (2005). The Storegga slide tsunami—Comparing field observations with numerical simulations. *Marine and Petroleum Geology*, 22(1), 195–208. <https://doi.org/10.1016/j.margeo.2004.10.003>
- Bonfardacci, A., Caruso, A., Bartolini, A., Bassinot, F., & Blanc-Valleron, M.-M. (2018). Distribution and ecology of the Globigerinoides ruber — Globigerinoides elongatus morphotypes in the Azores region during the late Pleistocene-Holocene. *Palaeogeography, Palaeoclimatology, Palaeoecology*, 491, 92–111. <https://doi.org/10.1016/j.palaeo.2017.11.052>
- Bryn, P., Berg, K., Forsberg, C., Solheim, A., & Kvalstad, T. (2005). Explaining the Storegga slide. *Marine and Petroleum Geology*, 22, 11–19. <https://doi.org/10.1016/j.margeo.2004.12.003>
- Canals, M., Lastras, G., Urgeles, R., Casamor, J. L., Mienert, J., Cattaneo, A., et al. (2004). Slope failure dynamics and impacts from seafloor and shallow sub-seafloor geophysical data: Case studies from the COSTA project. *Marine Geology*, 213(1–4), 9–72. <https://doi.org/10.1016/j.margeo.2004.10.001>
- Caress, D. W., & Chayes, D. N. (2017). MB-System: Mapping the seafloor. Retrieved from <https://www.mbari.org/products/research-software/mbsystem>
- Carter, L., Milliman, J. D., Talling, P. J., Gavey, R., & Wynn, R. B. (2012). Near-synchronous and delayed initiation of long run-out submarine sediment flows from a record-breaking river flood, offshore Taiwan. *Geophysical Research Letters*, 39(12), 1–5. <https://doi.org/10.1029/2012gl051172>
- Cropper, T. E., Hanna, E., & Bigg, G. R. (2014). Spatial and temporal seasonal trends in coastal upwelling off Northwest Africa, 1981–2012. *Deep Sea Research Part I: Oceanographic Research Papers*, 86, 94–111. <https://doi.org/10.1016/j.dsr.2014.01.007>
- Dan, G., Sultan, N., & Savoye, B. (2007). The 1979 Nice harbour catastrophe revisited: Trigger mechanism inferred from geotechnical measurements and numerical modelling. *Marine Geology*, 245(1–4), 40–64. <https://doi.org/10.1016/j.margeo.2007.06.011>
- Embley, R. W. (1976). New evidence for occurrence of debris flow deposits in the deep sea. *Geology*, 4(6), 371–374. [https://doi.org/10.1130/0091-7613\(1976\)4<371:Nefood>2.0.CO;2](https://doi.org/10.1130/0091-7613(1976)4<371:Nefood>2.0.CO;2)
- Embley, R. W. (1982). Anatomy of some Atlantic margin sediment slides and some comments on ages and mechanisms. In S. Saxov & J. K. Nieuwenhuis (Eds.), *Marine slides and other mass movements* (pp. 189–213). Springer US. https://doi.org/10.1007/978-1-4613-3362-3_11
- Embley, R. W., & Jacobi, R. D. (1977). Distribution and morphology of large submarine sediment slides and slumps on Atlantic continental margins. *Marine Geotechnology*, 2(1–4), 205–228. <https://doi.org/10.1080/10641197709379780>
- Fine, I. V., Rabinovich, A. B., Bornhold, B. D., Thomson, R. E., & Kulikov, E. A. (2005). The Grand Banks landslide-generated tsunami of November 18, 1929: Preliminary analysis and numerical modeling. *Marine Geology*, 215(1), 45–57. <https://doi.org/10.1016/j.margeo.2004.11.007>

- Flood, R. D. (1983). Classification of sedimentary furrows and a model for furrow initiation and evolution. *GSA Bulletin*, 94(5), 630–639. [https://doi.org/10.1130/0016-7606\(1983\)94<630:Cosfaa>2.0.Co;2](https://doi.org/10.1130/0016-7606(1983)94<630:Cosfaa>2.0.Co;2)
- Gatter, R., Clare, M. A., Kuhlmann, J., & Huhn, K. (2021). Characterisation of weak layers, physical controls on their global distribution and their role in submarine landslide formation. *Earth-Science Reviews*, 223, 103845. <https://doi.org/10.1016/j.earscirev.2021.103845>
- GEBCO Compilation Group (2020). GEBCO 2020 Grid. <https://doi.org/10.5285/a29c5465-b138-234d-e053-6c86abc040b9>
- Gee, M., Masson, D., Watts, A., & Allen, P. (1999). The Saharan debris flow: An insight into the mechanics of long runout submarine debris flows. *Sedimentology*, 46(2), 317–335. <https://doi.org/10.1046/j.1365-3091.1999.00215.x>
- Georgiopolou, A., Krastel, S., Masson, D. G., & Wynn, R. B. (2007). Repeated instability of the NW African margin related to buried landslide scarps. In V. Lykousis, D. Sakellariou, & J. Locat (Eds.), *Submarine mass movements and their consequences*, 3rd international symposium (pp. 29–36). Kluwer Academic Publishers. Retrieved from <http://www.scopus.com/inward/record.url?scp=84986197901&partnerID=8YFLogXK>
- Georgiopolou, A., Masson, D. G., Wynn, R. B., & Krastel, S. (2010). Sahara Slide: Age, initiation, and processes of a giant submarine slide. *Geochemistry, Geophysics, Geosystems*, 11(7), 1–22. <https://doi.org/10.1029/2010gc003066>
- Georgiopolou, A., Wynn, R. B., Masson, D. G., & Frenz, M. (2009). Linked turbidite–debride resulting from recent Sahara Slide headwall reactivation. *Marine and Petroleum Geology*, 26(10), 2021–2031. <https://doi.org/10.1016/j.marpetgeo.2009.02.013>
- Glimsdal, S., Pedersen, G. K., Harbitz, C. B., & Løvholt, F. (2013). Dispersion of tsunamis: Does it really matter? *Natural Hazards and Earth System Sciences*, 13(6), 1507–1526. <https://doi.org/10.5194/nhess-13-1507-2013>
- Grilli, S. T., Tappin, D. R., Carey, S., Watt, S. F. L., Ward, S. N., Grilli, A. R., et al. (2019). Modelling of the tsunami from the December 22, 2018 lateral collapse of Anak Krakatau volcano in the Sunda Straits, Indonesia. *Scientific Reports*, 9(1), 11946. <https://doi.org/10.1038/s41598-019-48327-6>
- Haflidason, H., Lien, R., Sejrup, H. P., Forsberg, C. F., & Bryn, P. (2005). The dating and morphometry of the Storegga Slide. *Marine and Petroleum Geology*, 22(1), 123–136. <https://doi.org/10.1016/j.marpetgeo.2004.10.008>
- Haflidason, H., Sejrup, H. P., Nygård, A., Mienert, J., Bryn, P., Lien, R., et al. (2004). The Storegga slide: Architecture, geometry and slide development. *Marine Geology*, 213(1), 201–234. <https://doi.org/10.1016/j.marpetgeo.2004.10.007>
- Hagen, E. (2001). Northwest African upwelling scenario. *Oceanologica Acta*, 24, 113–128. [https://doi.org/10.1016/S0399-1784\(00\)01110-5](https://doi.org/10.1016/S0399-1784(00)01110-5)
- Harbitz, C. B. (1992). Model simulations of tsunamis generated by the Storegga Slides. *Marine Geology*, 105(1), 1–21. [https://doi.org/10.1016/0025-3227\(92\)90178-K](https://doi.org/10.1016/0025-3227(92)90178-K)
- Harbitz, C. B., Løvholt, F., & Bungum, H. (2014). Submarine landslide tsunamis: How extreme and how likely? *Natural Hazards*, 72(3), 1341–1374. <https://doi.org/10.1007/s11069-013-0681-3>
- Hayes, D. E., Pimm, A. C., Beckmann, J. P., Benson, W. E., Berger, W. H., Roth, P. H., et al. (1972). DSDP Initial reports (Vol. 14).
- Hayes, D. E., & Rabinowitz, P. D. (1975). Mesozoic magnetic lineations and the magnetic quiet zone off northwest Africa. *Earth and Planetary Science Letters*, 28(2), 105–115. [https://doi.org/10.1016/0012-821x\(75\)90217-4](https://doi.org/10.1016/0012-821x(75)90217-4)
- Henrich, R., Hanebuth, T. J. J., Krastel, S., Neubert, N., & Wynn, R. B. (2008). Architecture and sediment dynamics of the Mauritania slide complex. *Marine and Petroleum Geology*, 25(1), 17–33. <https://doi.org/10.1016/j.marpetgeo.2007.05.008>
- Holz, C., Stuut, J.-b. W., & Henrich, R. (2004). Terrigenous sedimentation processes along the continental margin off NW Africa: Implications from grain-size analysis of seabed sediments. *Sedimentology*, 51(5), 1145–1154. <https://doi.org/10.1111/j.1365-3091.2004.00665.x>
- Hühnerbach, V., & Masson, D. G. (2004). Landslides in the north Atlantic and its adjacent seas: An analysis of their morphology, setting and behaviour. *Marine Geology*, 213(1–4), 343–362. <https://doi.org/10.1016/j.marpetgeo.2004.10.013>
- Krastel, S., Barrett, R., Gross, F., Gross, N., Jähmlich, H., Heinrich, S., et al. (2019). *Seismic pre-site survey for an IODP site on the Cape Verde Plateau. Cruise No. MSM87. 16.11.19 - 25.11.19, Las Palmas (Spain) - Mindelo (Cape Verde) (2195-8483)*. MARIA S. MERIAN-Berichte. Retrieved from https://www.tib.eu/de/suchen/id/awi%3Adoi%7E10.2312%252Fcr_msm87
- Krastel, S., Behrmann, J.-H., Völker, D., Stipp, M., Berndt, C., Urgeles, R., et al. (2014). *Submarine mass movements and their consequences*. (Vol. 37). In S. Krastel (Ed.). Springer. <https://doi.org/10.1007/978-3-319-00972-8>
- Krastel, S., Georgiopolou, A., Golbeck, I., Grün, M., Klauke, I., Mayer, M., et al. (2010). RV POSEIDON Fahrtbericht/Cruise report P395 Sahara slide complex 04.02-19.02.2010 las palmas-las palmas (Spain).
- Krastel, S., Kinne, S., Nitsche, F., Ahlers, J., Bischof, S., Bodenschatz, E., et al. (2019). *Morphology of the headwall area of the Sahara slide, NW-Africa, measuring over ocean references, mapping sequences to protists morphospecies from the Atlantic. Cruise No. MSM82/2, 26.04.19 - 14.05.19, Montevideo (Uruguay) - Las Palmas (Spain) (2195-8483)*. MARIA S. MERIAN-Berichte. Retrieved from https://www.tib.eu/de/suchen/id/awi%3Adoi%7E10.2312%252Fcr_msm82_2
- Krastel, S., Li, W., Urlaub, M., Georgiopolou, A., Wynn, R. B., Schwenk, T., et al. (2018). Mass wasting along the NW African continental margin. *Geological Society, London, Special Publications*, 477(1), 151–167. <https://doi.org/10.1144/sp477.36>
- Krastel, S., Wynn, R. B., Georgiopolou, A., Geersen, J., Henrich, R., Meyer, M., & Schwenk, T. (2012). Large-scale mass wasting on the north-west African continental margin: Some general implications for mass wasting on passive continental margins. In *Submarine mass movements and their consequences* (pp. 189–199). https://doi.org/10.1007/978-94-007-2162-3_17
- Kvalstad, T. J., Andresen, L., Forsberg, C. F., Berg, K., Bryn, P., & Wangen, M. (2005). The Storegga slide: Evaluation of triggering sources and slide mechanics. *Marine and Petroleum Geology*, 22(1–2), 245–256. <https://doi.org/10.1016/j.marpetgeo.2004.10.019>
- Laberg, J. S., & Camerlenghi, A. (2008). The significance of contourites for submarine slope stability. In M. Rebesco & A. Camerlenghi (Eds.), *Contourites* (Vol. 60, pp. 537–556). Elsevier. [https://doi.org/10.1016/s0070-4571\(08\)10025-5](https://doi.org/10.1016/s0070-4571(08)10025-5)
- Laberg, J. S., & Vorren, T. O. (2000). The Trænadjupet Slide, offshore Norway - Morphology, evacuation and triggering mechanisms. *Marine Geology*, 171(1), 95–114. [https://doi.org/10.1016/S0025-3227\(00\)00112-2](https://doi.org/10.1016/S0025-3227(00)00112-2)
- Lee, H. J. (2009). Timing of occurrence of large submarine landslides on the Atlantic Ocean margin. *Marine Geology*, 264(1–2), 53–64. <https://doi.org/10.1016/j.marpetgeo.2008.09.009>
- Li, W., Alves, T. M., Urlaub, M., Georgiopolou, A., Klauke, I., Wynn, R. B., et al. (2017). Morphology, age and sediment dynamics of the upper headwall of the Sahara slide complex, northwest Africa: Evidence for a large late Holocene failure. *Marine Geology*, 393, 109–123. <https://doi.org/10.1016/j.marpetgeo.2016.11.013>
- Lindberg, B., Laberg, J. S., & Vorren, T. O. (2004). The Nyk Slide - Morphology, progression, and age of a partly buried submarine slide offshore northern Norway. *Marine Geology*, 213(1–4), 277–289. <https://doi.org/10.1016/j.marpetgeo.2004.10.010>
- Locat, J., Leroueil, S., Locat, A., & Lee, H. (2014). Weak layers: Their definition and classification from a geotechnical perspective. In S. Krastel, J.-H. Behrmann, D. Völker, M. Stipp, C. Berndt, R. Urgeles, et al. (Eds.), *Submarine mass movements and their consequences* (pp. 3–12). Springer International Publishing. https://doi.org/10.1007/978-3-319-00972-8_1
- Løvholt, F., Pedersen, G., Harbitz, C. B., Glimsdal, S., & Kim, J. (2015). On the characteristics of landslide tsunamis. *Philosophical Transactions of the Royal Society A: Mathematical, Physical & Engineering Sciences*, 373(2053), 20140376. <https://doi.org/10.1098/rsta.2014.0376>

- Løvholt, F., Schulten, I., Mosher, D., Harbitz, C., & Krastel, S. (2018). Modelling the 1929 Grand Banks slump and landslide tsunami. In D. G. Lintern, D. C. Mosher, L. G. Moscardelli, P. T. Bobrowsky, C. Campbell, J. Chaytor, et al. (Eds.), *Subaqueous mass movements and their consequences: Assessing geohazards, environmental implications and economic significance of subaqueous landslides* (Vol. 477, pp. 315–331). The Geological Society of London. <https://doi.org/10.1144/sp477.28>
- Mangerud, J., & Gulliksen, S. (1975). Apparent radiocarbon ages of recent marine shells from Norway, spitsbergen, and Arctic Canada. *Quaternary Research*, 5(2), 263–273. [https://doi.org/10.1016/0033-5894\(75\)90028-9](https://doi.org/10.1016/0033-5894(75)90028-9)
- Masson, D. G., Harbitz, C. B., Wynn, R. B., Pedersen, G., & Lovholt, F. (2006). Submarine landslides: Processes, triggers and hazard prediction. *Philos Trans A Math Phys Eng Sci*, 364(1845), 2009–2039. <https://doi.org/10.1098/rsta.2006.1810>
- Masson, D. G., Huggett, Q. J., & Brunson, D. (1993). The surface texture of the Saharan Debris Flow deposit and some speculations on submarine debris flow processes. *Sedimentology*, 40(3), 583–598. <https://doi.org/10.1111/j.1365-3091.1993.tb01351.x>
- Masson, D. G., Watts, A. B., Gee, M. J. R., Urgeles, R., Mitchell, N. C., Le Bas, T. P., & Canals, M. (2002). Slope failures on the flanks of the Western Canary islands. *Earth-Science Reviews*, 57(1–2), 1–35. [https://doi.org/10.1016/S0012-8252\(01\)00069-1](https://doi.org/10.1016/S0012-8252(01)00069-1)
- McAdoo, B. G., Pratson, L. F., & Orange, D. L. (2000). Submarine landslide geomorphology, US continental slope. *Marine Geology*, 169(1), 103–136. [https://doi.org/10.1016/S0025-3227\(00\)00050-5](https://doi.org/10.1016/S0025-3227(00)00050-5)
- Micallef, A., Masson, D. G., Berndt, C., & Stow, D. A. V. (2007). Morphology and mechanics of submarine spreading: A case study from the Storegga slide. *Journal of Geophysical Research*, 112(F3), F03023. <https://doi.org/10.1029/2006jf000739>
- Müller, P. J., & Suess, E. (1979). Productivity, sedimentation rate, and sedimentary organic matter in the oceans—I. Organic carbon preservation. *Deep-Sea Research, Part A: Oceanographic Research Papers*, 26(12), 1347–1362. [https://doi.org/10.1016/0198-0149\(79\)90003-7](https://doi.org/10.1016/0198-0149(79)90003-7)
- Pakoksung, K., Suppasri, A., Imamura, F., Athanasius, C., Omang, A., & Muhari, A. (2019). Simulation of the submarine landslide tsunami on 28 September 2018 in Palu Bay, Sulawesi island, Indonesia, using a two-layer model. *Pure and Applied Geophysics*, 176(8), 3323–3350. <https://doi.org/10.1007/s00024-019-02235-y>
- Piper, D. J. W., Cochonat, P., & Morrison, M. L. (1999). The sequence of events around the epicentre of the 1929 Grand Banks earthquake: Initiation of debris flows and turbidity current inferred from sidescan sonar. *Sedimentology*, 46(1), 79–97. <https://doi.org/10.1046/j.1365-3091.1999.00204.x>
- Piper, D. J. W., Cochonat, P., & Morrison, M. L. (2002). The sequence of events around the epicentre of the 1929 Grand Banks earthquake: Initiation of debris flows and turbidity current inferred from sidescan sonar. *Sedimentology*, 46(1), 79–97. <https://doi.org/10.1046/j.1365-3091.1999.00204.x>
- Reimer, P. J., Bard, E., Bayliss, A., Beck, J. W., Blackwell, P. G., Ramsey, C. B., et al. (2013). IntCal13 and Marine13 radiocarbon age calibration curves 0–50,000 Years cal BP. *Radiocarbon*, 55(4), 1869–1887. https://doi.org/10.2458/azu_js_rc.55.16947
- Ruddiman, W., Sarnthein, M., Baldauf, J., Backman, J., Bloemendal, J., Curry, W., et al. (1988). *Proceedings of the Ocean Drilling Program, Initial Reports* (Vol. 108, pp. 31–104). Ocean Drilling Program. <https://doi.org/10.2973/odp.proc.ir.108.102.1988>
- Sarnthein, M., Thiede, J., Pflaumann, U., Erlenkeuser, H., Fütterer, D., Koopmann, B., et al. (1982). Atmospheric and oceanic circulation patterns off northwest Africa during the past 25 million years. In *Geology of the northwest African continental margin*. (pp. 545–604). Springer.
- Scarselli, N. (2020). Chapter 16 - submarine landslides – Architecture, controlling factors and environments. A summary. In N. Scarselli, J. Adam, D. Chiarella, D. G. Roberts, & A. W. Bally (Eds.), *Regional geology and tectonics* (2nd edn.) (pp. 417–439). Elsevier. <https://doi.org/10.1016/B978-0-444-64134-2.00015-8>
- Schambach, L., Grilli, S. T., & Tappin, D. R. (2021). New high-resolution modeling of the 2018 Palu tsunami, based on supershear earthquake mechanisms and mapped coastal landslides. *Frontiers of Earth Science*, 8, 598839. <https://doi.org/10.3389/feart.2020.598839>
- Schulten, I., Mosher, D. C., Piper, D. J. W., & Krastel, S. (2019). A massive slump on the St. Pierre slope, A new perspective on the 1929 Grand Banks submarine landslide. *Journal of Geophysical Research: Solid Earth*, 124(8), 7538–7561. <https://doi.org/10.1029/2018jb017066>
- Schulz, H., Ait Chatou, M., Antobreh, A. A., Enneking, K., Esper, O., Fabian, K., et al. (2003). Report and preliminary results of meteor cruise M 58/1, Dakar - las palmas, 15.04. - 12.05.2003. Retrieved from <http://elib.suub.uni-bremen.de/ip/docs/00010336.pdf>
- Schulz, H. D., & Hanebuth, T. J. J. (2003). Documentation of sediment core GeoB8533-4 PANGAEA. <https://doi.org/10.1594/PANGAEA.128903>
- Shackleton, N. J., Hall, M. A., & Vincent, E. (2000). Phase relationships between millennial-scale events 64, 000–24, 000 years ago. *Paleoceanography*, 15(6), 565–569. <https://doi.org/10.1029/2000PA000513>
- Summerhayes, C. P., Milliman, J. D., Briggs, S. R., Bee, A. G., & Hogan, C. (1976). Northwest African shelf sediments: Influence of climate and sedimentary processes. *The Journal of Geology*, 84(3), 277–300. <https://doi.org/10.1086/628196>
- Talling, P. J., Wynn, R. B., Masson, D. G., Frenz, M., Cronin, B. T., Schiebel, R., et al. (2007). Onset of submarine debris flow deposition far from original giant landslide. *Nature*, 450(7169), 541–544. <https://doi.org/10.1038/nature06313>
- Tang, Q., & Krastel, S. (2022). Multibeam, echosounder and gravity cores data of the headwall area in the Sahara Slide Complex. *PANGAEA*. <https://doi.org/10.1594/PANGAEA.943644>
- Tappin, D. R., Watts, P., & Grilli, S. T. (2008). The Papua New Guinea tsunami of 17 July 1998: Anatomy of a catastrophic event. *Natural Hazards and Earth System Sciences*, 8(2), 243–266. <https://doi.org/10.5194/nhess-8-243-2008>
- Tappin, D. R., Watts, P., McMurtry, G. M., Lafoy, Y., & Matsumoto, T. (2001). The Sissano, Papua New Guinea tsunami of July 1998 - Offshore evidence on the source mechanism. *Marine Geology*, 175(1), 1–23. [https://doi.org/10.1016/S0025-3227\(01\)00131-1](https://doi.org/10.1016/S0025-3227(01)00131-1)
- Urlaub, M., Geersen, J., Krastel, S., & Schwenk, T. (2018). Diatom ooze: Crucial for the generation of submarine mega-slides? *Geology*, 46(4), 331–334. <https://doi.org/10.1130/g39892.1>
- Urlaub, M., Talling, P. J., & Masson, D. G. (2013). Timing and frequency of large submarine landslides: Implications for understanding triggers and future geohazard. *Quaternary Science Reviews*, 72, 63–82. <https://doi.org/10.1016/j.quascirev.2013.04.020>
- Urlaub, M., Talling, P. J., Zervos, A., & Masson, D. (2015). What causes large submarine landslides on low gradient (<2°) continental slopes with slow (~0.15 m/kyr) sediment accumulation. *Journal of Geophysical Research: Solid Earth*, 120(10), 6722–6739. <https://doi.org/10.1002/2015jb012347>
- von Rad, U., Hinz, K., Sarnthein, M., & Seibold, E. (1982). *Geology of the northwest African continental margin*. Springer Science & Business Media. <https://doi.org/10.1007/978-3-642-68409-8>
- Ward, S. N. (2001). Landslide tsunami. *Journal of Geophysical Research*, 106(B6), 11201–11215. <https://doi.org/10.1029/2000JB900450>
- Weaver, P. P. E., Wynn, R. B., Kenyon, N. H., & Evans, J. (2000). Continental margin sedimentation, with special reference to the north-east Atlantic margin. *Sedimentology*, 47(s1), 239–256. <https://doi.org/10.1046/j.1365-3091.2000.0470s1239.x>
- Wynn, R. B., Masson, D. G., Stow, D. A. v., & Weaver, P. P. e. (2000). The Northwest African slope apron: A modern analogue for deep-water systems with complex seafloor topography. *Marine and Petroleum Geology*, 17(2), 253–265. [https://doi.org/10.1016/S0264-8172\(99\)00014-8](https://doi.org/10.1016/S0264-8172(99)00014-8)
- Zhang, W., Klein, B., Randolph, M. F., & Puzrin, A. M. (2021). Upslope failure mechanisms and criteria in submarine landslides: Shear band propagation, slab failure and retrogression. *Journal of Geophysical Research: Solid Earth*, 126(9), e2021JB022041. <https://doi.org/10.1029/2021JB022041>